Title

A Study of the Flowfield Evolution and Mixing in a Planar Turbulent Jet Using Direct Numerical Simulation

Authors

Stanley, S A

Sarkar, S

Publication Date

1999-03-01

LBNL-43005
Preprint

ERNEST ORLANDO LAWRENCE
BERKELEY NATIONAL LABORATORY

A Study of the Flowfield Evolution and Mixing in a Planar Turbulent Jet Using Direct Numerical Simulation

S.A. Stanley and S. Sarkar

National Energy Research
Scientific Computing Division

March 1999

Submitted to
Journal of
Fluid Mechanics

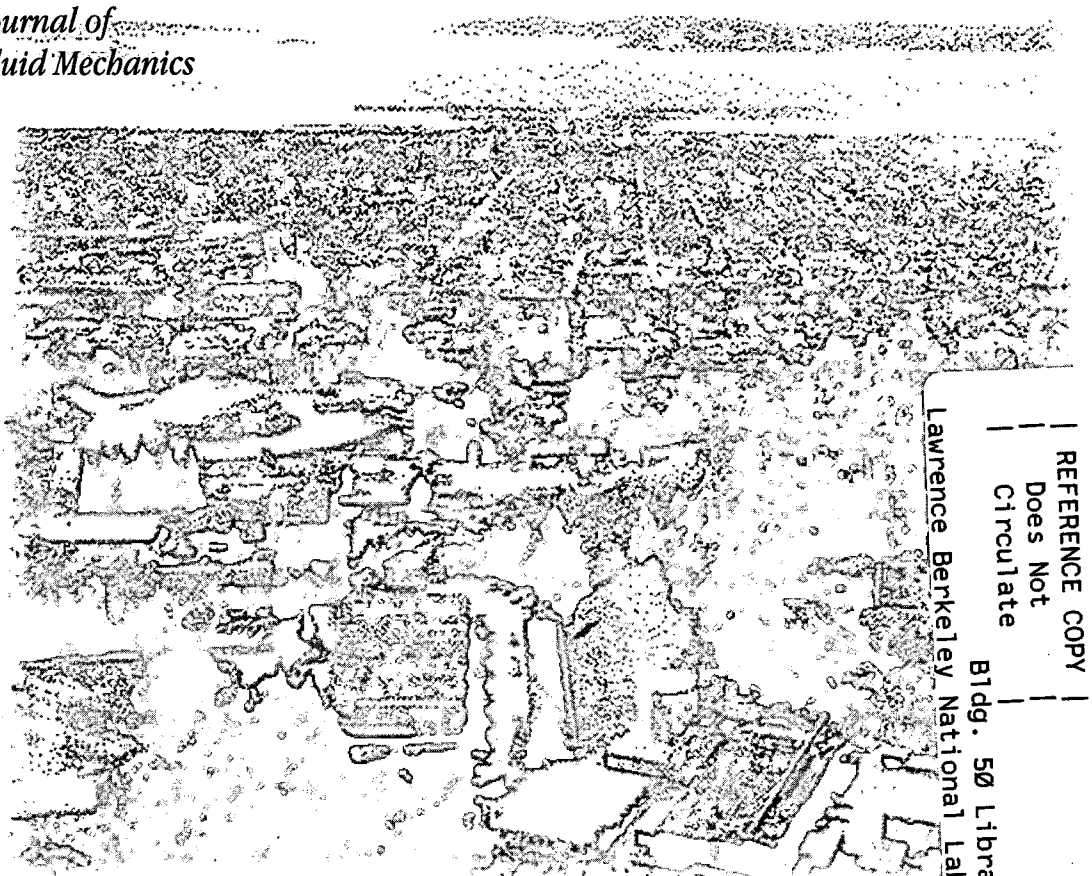

DISCLAIMER

LBNL-43005

A Study of the Flowfield Evolution and Mixing in a Planar Turbulent Jet Using Direct Numerical Simulation

S.A. Stanley

National Energy Research Scientific Computing Division
Ernest Orlando Lawrence Berkeley National Laboratory
University of California
Berkeley, California 94720

and

S. Sarkar

University of California, San Diego
La Jolla, California 92093-0411

March 1999

This work was supported in part by the Office of Energy Research, Applied Mathematical Sciences Program of the Office of Mathematics, Information, and Computational Sciences, of the U.S. Department of Energy under Contract No. DE-AC03-76SF00098, and AFOSR through Grant No. F49620-96-1-0106.

A study of the flowfield evolution and mixing in a planar turbulent jet using direct numerical simulation

S. A. Stanley[1,2] and S. Sarkar[1]

[1]University of California, San Diego, La Jolla, CA 92093-0411

[2]current address, Lawrence Berkeley National Laboratory, 50A-1148, Berkeley, CA 94720

Abstract

Turbulent plane jets are prototypical free shear flows of practical interest in propulsion, combustion and environmental flows. While considerable experimental research has been performed on planar jets, very few computational studies exist. To the author's knowledge, this is the first computational study of three-dimensional planar turbulent jets utilizing direct numerical simulation.

A validation of the results from the direct numerical simulation against experimental data is shown. Jet growth rates as well as the self-similar mean velocity, mean scalar and Reynolds stress profiles all compare well with experimental data. Coherency spectra, vorticity visualization and autospectra are obtained to identify inferred structures. The development of the initial shear layer instability, as well as the evolution into the jet column mode downstream is captured well.

A detailed analysis of the large- and small-scale anisotropies in the jet is discussed. It is shown that while the large-scales in the flowfield adjust slowly to variations in the local mean velocity gradients, the small-scales adjust rapidly. Near the centerline of the jet, the small-scales of turbulence are more isotropic.

The evolution of the mixing process in turbulent planar jets is studied through analysis of the probability density functions of a passive scalar. Immediately after the roll up of vortical structures in the shear layers, the mixing process is dominated by large-scale engulfing of fluid. However, small-scale mixing dominates further downstream in the turbulent core of the self-similar region of the jet and a change from nonmarching to marching PDFs is observed. Near the jet edges, the effects of large-scale engulfing of coflow fluid continue to influence the PDFs and non-marching type behavior is observed.

1 Introduction

Turbulent plane jets are prototypical free shear flows on which fundamental research can expand the overall understanding of the characteristics of turbulent flows. In addition, turbulent plane jets are of practical interest due to their presence in a broad range of engineering applications such as combustion, propulsion, and environmental flows. A thorough understanding of the dynamics of these flows is required in order to understand and control the transport processes in these applications.

There are a number of issues in planar turbulent jets still requiring further research. For instance, the development of large and small-scale structures, their mutual interaction, and the response to external forcing are current topics of investigation in jets. The evolution from the initial shear layer modes to the jet column mode downstream is also of interest. While the fully developed "self-similar" region downstream is of fundamental interest, the large-scale structural reorganization in the nearfield of planar jets and the subsequent impact on the evolution of turbulence and mixing in the first ten to twenty jet widths is of great practical interest. For example, mixing in combustion and noise generation in propulsion are both applications for which the initial region of the jet is important.

The intent of this research has been to develop an accurate computational model of a spatially evolving turbulent plane jet that is rigorously validated against experimental data. Such a model could then be utilized to study the fundamental as well as practical issues in the development of these flowfields. Towards this end, direct numerical simulation, DNS, of the full Navier-Stokes equations has been utilized in order to eliminate the uncertainties added by the inclusion of a model for the turbulent stresses. DNS has been utilized in the study of free turbulent shear flows which are homogeneous in one or more directions, that is, temporal simulations. However, relatively few direct numerical simulations of spatially evolving turbulent flows have been performed. To the authors' knowledge, no direct numerical simulation of planar turbulent jets has been performed outside of the current study.

1.1 A Historical Summary of Planar Jet Research

Many experimental studies have been performed on planar turbulent jets. The early study by Albertson *et al.* (1950) concentrated on the measurement of mean velocity profiles in planar and circular turbulent jets. With the advent of hot-wire anemometry, later studies were able to focus on quantifying the statistical quantities related not only to the mean flowfields, but also to the fluctuating fields. Miller & Comings (1957) measured the mean velocity and pressure fields, as well as the Reynolds stresses in the first forty jet widths. Later work of Bradbury (1965), Heskestad (1965), and Gutmark & Wygnanski (1976) used hot-wire anemometry to measure the mean and Reynolds stress profiles in the self-similar region of planar jets. It was found through these experiments that the evolution of the fluctuating velocity fields as well as the jet spreading rate and centerline velocity decay were strongly affected by the initial conditions at the nozzle and the external conditions in the laboratory. Everitt & Robins (1978), Bradbury & Riley (1967) as well as recent work of LaRue *et al.* (1997) showed that the presence of a strong coflow can slow the development of the jet to a self-similar state.

With the practical applications of turbulent buoyant jets, such as in smoke stacks and cooling water discharges from power-plants, there was considerable interest in the effects of buoyancy and heat transfer in planar jets. Bashir & Uberoi (1975), Kotsovinos (1977) as well as Kotsovinos & List (1977) studied the effects of buoyancy and heat transfer in highly heated jets, while Jenkins & Goldschmidt (1973), Davies, Keffer & Baines (1975) and Browne *et al.* (1983) studied mixing of the temperature field in more moderately heated jets.

In general, the early work on planar jets concentrated on the study of the statistical quantities in the flowfield. However, correlation measurements in the jet led to an increased interest in the large-scale coherent motions. Lateral correlation measurements, across the jet, of Goldschmidt & Bradshaw (1973) exhibited quasi-periodicity in time, and showed negative correlation of the longitudinal velocity at zero time delay, while profiles of the autocorrelation coefficient of the longitudinal velocity across the jet by Gutmark & Wygnanski (1976) and Everitt & Robins (1978) showed negative lobes for large probe separations. These measurements were originally interpreted as indicating a large-scale, flag-like, flapping motion in the self-similar region of the jet.

Later Cervantes de Gortari & Goldschmidt (1981) observed that the apparent "flapping" frequency scaled with the large-scale properties of the jet and corresponded with the frequency of the structures responsible for intermittency. Based on these observations they concluded that the correlation measurements were a result of large-scale structures in the jet rather than a flapping motion. Utilizing further correlation measurements, Oler & Goldschmidt (1982) suggested that a two-dimensional, asymmetric, von Kármán-like vortex street existed. They verified, using numerical simulations, that this structure could produce the observed correlations. Further studies by Mumford (1982), Antonia *et al.* (1983), Goldschmidt, Moallemi & Oler (1983), as well as Oler & Goldschmidt (1984) have supported this structural arrangement in the flow. Mumford (1982), however, suggested that the von Kármán-like vortex street might also be accompanied by roller-like structures aligned in the direction of mean strain. The size of these structures was shown to scale

in a manner consistent with the self-preserving nature of the plane jet.

Early work of Sato (1960) and Rockwell & Niccolls (1972), as well as later work of Antonia *et al.* (1983) and Thomas & Goldschmidt (1986*b*) have shown that near the nozzle, the structures are predominately symmetrical, for a flat exit velocity profile. This "varicose" mode is most commonly observed in the nearfield of planar jets. Michalke & Freymuth (1966) showed that very near the nozzle lip, the growth of instabilities in the shear layers on plane jets closely followed that predicted by a spatial stability analysis for the shear layer. The evolution from this symmetric configuration near the nozzle lip to the asymmetric structure in the fully developed region of the jet is not fully understood. Antonia *et al.* (1983) found that this transition occurs in the region after the merging of the shear layers, but before similarity is achieved. It is in this region that the mean velocity profile changes from a relatively flat profile to a curved profile. Sato (1960) and Rockwell & Niccolls (1972) showed that asymmetric structures in the jet are characteristic of a curved mean velocity profile. Likewise, for jets evolving from a curved velocity profile in the nozzle an asymmetric or "sinuous" mode is observed in the nearfield of the jet.

Thomas & Goldschmidt (1986*a*,*b*) studied the growth and development of large-scale structures in the initial region of naturally developing planar turbulent jets. They identified symmetric and antisymmetric modes in the near field of the jet and suggested that the antisymmetric modes were due to a resonant forcing of the shear layers by the jet structures downstream of the potential core. Thomas & Chu (1989) further studied the evolution of the near field of the jet by imposing a low level acoustic forcing upstream of the nozzle to organize the initial instability wave in order to facilitate it's study. They were able to further confirm the upstream feedback and suggested that it was a result of the loss of symmetry of the large-scale structures downstream of the potential core. Thomas & Prakash (1991) studied the evolution of the shear layer modes to the jet column mode in an "untuned" jet, where the standard shear layer progression of subharmonic growth is incapable of obtaining the jet mode, $f^*_{jt} \neq f^*_{sl}/2^n$. They observed a drastically different spectral evolution than is observed through the subharmonic instability, occurring symmetrically in the jet shear layers. This evolution was followed by a rapid loss of symmetry in the region just downstream of the potential core.

Most of the more recent work on planar jets has concentrated on the evolution from the shear layer dominated region near the nozzle to the jet region downstream, as well as on the characteristics of the large-scale structures in the fully developed region of the jet. However, there have been a few exceptions. Ramaprian & Chandrasekhara (1985) revisited the statistics in the fully developed region of the jet using laser Doppler anemometry, while Lemieux & Oosthuizen (1985) and Namer & Ötügen (1988) studied the effects of Reynolds number on the initial development of planar turbulent jet.

1.2 Numerical Studies on Turbulent Plane Jets

There have been considerably fewer numerical studies of plane jets than experimental. Oler & Goldschmidt (1982) tested the idea of a von Kármán-like vortex street, by simulating the fully developed region of a two-dimensional jet as a spatially growing vortex street composed of a superposition of Rankine vortices. The downstream growth was prescribed in order to match the self-similar growth observed in experiments. Comte *et al.* (1989) performed direct temporal simulations of the fully developed region of a two-dimensional Bickley jet. For simulations initialized with a white noise perturbation, a von Kármán-like vortex street developed and exhibited pairing between vortices of like sign. However, when the initial stream function contained a sine perturbation in the streamwise direction at the fundamental mode, the vortex street developed, but the subsequent pairing was inhibited. Dai, Kobayashi & Taniguchi (1994) performed the first simulations of a spatially evolving, subsonic, plane jet. Unlike the DNS approach used here, they performed large-eddy simulations of an incompressible, three-dimensional, plane turbulent jet using a Smagorinsky model. They obtained relatively good agreement with experimental data in their mean profiles, however the

self-similar turbulence intensities were 40% high. Similarly, Weinberger, Rewerts & Janicka (1997) showed self-similar fluctuation intensities which were 15% high in their large-eddy simulation of a spatially evolving, incompressible, plane jet using the Smagorinsky model. However, neither of these studies analyzed the influence of the LES model utilized. Le Ribault, Sarkar & Stanley (1998) performed an extensive comparison of the Smagorinsky, dynamic Smagorinsky and dynamic mixed LES models in simulations of the near field region of planar turbulent jets. They found that while the dynamic models worked well, the standard Smagorinsky model severely underestimated the initial growth and turbulence development in the near field of the jet.

Reichert & Biringen (1997) studied the effects of compressibility on the spatial evolution of two-dimensional, inviscid jets with a strong coflow. While their jets were slow to develop, they did observe self-similar growth rates downstream. They showed a reduction in the jet growth rate and entrainment with increasing convective Mach number, $M_c = (U_1 - U_2)/(c_1 + c_2)$. For $M_c = 0.4$, they observed a sharp decrease in the entrainment in the self-similar region of the jet. In addition to these simulations of free planar jets, Hoffmann & Benocci (1994) performed a large-eddy simulation of a planar jet impinging on a wall while Jones & Wille (1996) performed a LES of a plane jet into a cross-flowing stream.

Stanley & Sarkar (1997*a*,*b*) performed comparisons of two-dimensional weak and strong jets with three-dimensional jets in an attempt to determine the usefulness of two-dimensional simulations in the study of planar jets. In agreement with Reichert & Biringen it was found that two-dimensional jets with a strong coflow velocity, "weak jets", evolved significantly slower than experimentally observed planar jets. In addition, two-dimensional jets with a weak coflow, "strong jets", behave in a fashion totally unlike experimentally observed jets, with differences in even the mean profiles. This was a result of a two-dimensional instability in symmetric and asymmetric vortex streets.

Stanley & Sarkar (1999) studied the influence of the inflow fluctuation intensity and the shear layer thickness, as well as the effects of discrete forcing, on the initial development of planar turbulent jets. They found that the inflow fluctuation intensity and shear layer momentum thickness had a strong influence on the jet development, with higher fluctuation intensity and thinner shear layers leading to more rapid jet development and an asymptotic approach of the centerline turbulent kinetic energy to the self-similar values. Lower fluctuation intensity and thicker shear layers generated overshoots in the centerline turbulent kinetic energy. Two-dimensional discrete forcing at the fundamental and first subharmonic mode of the shear layers enhanced the growth of the large-scale structures in the initial region of the jet. However, the influence of discrete forcing was rapidly lost downstream with the breakdown of the large-scale structures.

2 Mathematical Description

2.1 Governing Equations

The governing equations applicable in the study of compressible, turbulent shear flows consist of the conservation equations for mass, momentum and energy. In this study we assume an ideal gas with a Newtonian relationship between fluid stress and rate of strain. The nondimensional conservation equations are summarized below.

Mass conservation:

$$\frac{\partial \rho}{\partial t} + \frac{\partial (\rho u_k)}{\partial x_k} = 0 \tag{1}$$

Momentum conservation:

$$\frac{\partial (\rho u_i)}{\partial t} + \frac{\partial (\rho u_i u_k)}{\partial x_k} = -\frac{\partial p}{\partial x_i} + \frac{1}{Re}\frac{\partial \tau_{ij}}{\partial x_j} \tag{2}$$

where the viscous stress tensor, τ_{ij}, is given by

$$\tau_{ij} = \left(\frac{\partial u_i}{\partial x_j} + \frac{\partial u_j}{\partial x_i}\right) - \frac{2}{3}\frac{\partial u_k}{\partial x_k}\delta_{ij} \tag{3}$$

Energy conservation:

$$\frac{\partial p}{\partial t} + u_k\frac{\partial p}{\partial x_k} + \gamma p\frac{\partial u_k}{\partial x_k} = \frac{\gamma}{PrRe}\frac{\partial^2 T}{\partial x_k^2} + \frac{\gamma - 1}{Re}\Phi \tag{4}$$

where Φ is the viscous dissipation function,

$$\Phi = \tau_{ij}\frac{\partial u_i}{\partial x_j} \tag{5}$$

The values of the fluid thermodynamic quantities are related through the equation of state for an ideal gas,

$$p = \rho RT \tag{6}$$

In these expressions, density, velocity, pressure, temperature, length and time are normalized by the reference quantities ρ_r, u_r, $p_r = \rho_r u_r^2$, $T_r = p_r/(\rho_r R_r)$, l_r, and $t_r = l_r/u_r$, respectively.

Additionally, a scalar equation is included which expresses the conservation of a passive property, ξ,

$$\frac{\partial(\rho\xi)}{\partial t} + \frac{\partial(\rho u_k \xi)}{\partial x_k} = \frac{1}{ReSc}\frac{\partial}{\partial x_k}\left(\rho\frac{\partial \xi}{\partial x_k}\right) \tag{7}$$

The property ξ is passive in that it is influenced by the other properties of the flowfield, however it has no influence on the flow itself. This type of passive scalar equation is commonly used to study mixing in turbulent shear flows and is applicable to chemical systems under the assumption of infinitely fast chemistry, a useful simplification (Williams, 1985) in combustion studies.

2.2 Favre Decomposition of the Flow Field

The most common averaging procedure in the study of turbulent compressible flows utilizes mass-weighted Favre averages. The advantage of using the mass-weighted decomposition over the standard Reynolds decomposition is the ensuing simplified form of the averaged convective transport terms in the conservation equations. For any variable ϕ, $\widetilde{\phi}$ denotes the Favre average and ϕ'' the corresponding fluctuation, while $\overline{\phi}$ denotes the Reynolds average and ϕ' the corresponding fluctuation.

The Favre-averaged momentum equations are

$$\frac{\partial(\overline{\rho}\widetilde{u}_i)}{\partial t} + \frac{\partial(\overline{\rho}\widetilde{u}_i\widetilde{u}_j)}{\partial x_j} = -\frac{\partial \overline{p}}{\partial x_i} + \frac{1}{Re}\frac{\partial \overline{\tau_{ij}}}{\partial x_j} - \frac{\partial(\overline{\rho}R_{ij})}{\partial x_j} \tag{8}$$

where

$$\overline{\tau_{ij}} = \overline{\left(\frac{\partial u_i}{\partial x_j} + \frac{\partial u_j}{\partial x_i}\right)} - \frac{2}{3}\frac{\partial \overline{u_k}}{\partial x_k}\delta_{ij} \tag{9}$$

and $R_{ij} = \widetilde{u_i''u_j''}$ is the Favre-averaged Reynolds stress tensor. The equation for the turbulent kinetic energy, $K = R_{kk}/2$, is given by

$$\frac{\partial K}{\partial t} + \widetilde{u}_j\frac{\partial K}{\partial x_j} = P^* - \epsilon^* - \frac{1}{\overline{\rho}}\frac{\partial T_j^*}{\partial x_j} + \frac{1}{\overline{\rho}}\Pi^* - \frac{1}{\overline{\rho}}\Delta^* + \frac{1}{\overline{\rho}}V^* \tag{10}$$

where the turbulence production is,

$$P^* = -R_{jk}\frac{\partial \widetilde{u_j}}{\partial x_k} \tag{11}$$

the turbulent dissipation rate is,

$$\epsilon^* = \frac{1}{\overline{\rho} Re}\overline{\tau'_{jk}\frac{\partial u'_j}{\partial x_k}} \tag{12}$$

the turbulent transport is,

$$T_j^* = \frac{1}{2}\overline{\rho u''_k u''_k u''_j} + \overline{u'_k p'}\delta_{kj} - \frac{1}{Re}\overline{u'_k \tau'_{jk}} \tag{13}$$

the pressure-dilatation is,

$$\Pi^* = \overline{p'\frac{\partial u'_k}{\partial x_k}} \tag{14}$$

while the last two terms,

$$\Delta^* = \overline{u''_j}\frac{\partial \overline{p}}{\partial x_j} \tag{15}$$

and

$$V^* = \frac{1}{Re}\overline{u''_j}\frac{\partial \overline{\tau_{jk}}}{\partial x_k} \tag{16}$$

are a result of density variations.

3 Numerical Techniques

In this section the techniques used in this study to numerically solve the equations for conservation of mass, momentum and energy, § 2.1, are summarized. Further details may be found in Stanley & Sarkar (1999). The general requirements for any study of turbulence using direct numerical simulation is that the numerical techniques provide high accuracy in both space and time as well as be computationally efficient. Through the development of the numerical algorithm described below a balance between accuracy and efficiency was sought.

The Euler terms in the governing equations discussed in § 2.1 are marched in time using the low-storage, fourth-order Runge-Kutta integration scheme of Carpenter & Kennedy (1994). The viscous and conduction terms are marched in time using a first-order integration scheme. This is implemented by advancing the Euler terms in time using the Runge-Kutta scheme described above and then evaluating and advancing the viscous terms using a first-order scheme. The advantage of this approach is that 20% less computational work is required for each time step than for a full Runge-Kutta time advance of all terms. It was discovered through the course of this investigation that, for the conditions being studied, treating the viscous and conduction terms in this way had a negligible impact on the accuracy of the solution.

A nonuniform fourth-order compact derivative scheme is utilized to evaluating the spatial derivatives. This scheme generalizes the uniform compact derivatives of Lele (1992) to nonuniform meshes. This central-derivative scheme is closed at the boundaries using internal-biased, nonuniform, third-order compact derivatives based on the uniform derivatives of Carpenter, Gottlieb & Abarbanel (1993). This 3-4-3 scheme allows the simulation of problems on an open, non-periodic, domain

while maintaining an overall fourth-order spatial accuracy in the physical coordinate Δx on the nonuniform grid. In order to eliminate high wave-number errors resulting from numerical boundary closures, a nonuniform fourth-order compact filter is utilized to damp the high wave-number modes. As with the compact derivatives, this nonuniform compact filter generalizes the uniform filter of Lele (1992) to nonuniform meshes providing fourth-order accuracy in Δx. Only modes between the highest wave-number, $k_x = 0.5\Delta x$, and $k_x = 0.43\Delta x$ are significantly affected by the filter. The jet Reynolds number and grid resolution are chosen such that filtering does not remove dynamically significant scales of motion.

The solution of the governing equation for the passive scalar, equation 7, is based on the flux-corrected-transport, FCT, scheme of Zalesak (1979). The predictor stage is performed with a low-order scheme, 1st-order upwind, which produces a monotone solution. The corrector stage then modifies the predicted solution using the difference between a high-order scheme, 4th-order compact evaluation, and the low order scheme. This correction is nonlinearly limited so that the numerical solution is always bound between the known minimum of $\xi = 0.0$ and maximum of $\xi = 1.0$ avoiding spurious numerical oscillations. Sufficient resolution is used so that scalar statistics are obtained accurately.

One of the greatest difficulties in the simulation of spatially evolving flows is the formulation of boundary conditions required due to the truncation of the infinite physical domain to a finite region containing the portion of the flowfield which is of interest. At the subsonic inflow boundary, the governing equations are essentially solved in a characteristic form. The time variations of the incoming characteristic variables are specified while the equation for the outgoing characteristic variable is solved using internal biased derivatives. Through the solution of the equation for the outgoing acoustics, the actual values of the variables at the inflow plane are allowed to float around the specified "target" values thus avoiding sharp changes during the downstream evolution as well as introduction of excessive dilatation, $\nabla \cdot \mathbf{u}$, into the flow. In addition, a simple exponential damping term is introduced into the governing equations for the streamwise momentum and the passive scalar at the inflow plane. Written for the passive scalar equation, this term is of the form

$$\frac{\partial \xi}{\partial t} = \text{Standard Terms} - \sigma \left(\xi - \overline{\xi} \right) \tag{17}$$

where $\sigma = 0.22$. These weak damping terms are added to counteract the long time effects of the weak numerical diffusion on the inflow profiles and maintain steady target mean profiles while, at the same time, allowing the desired fluctuation intensity about this mean. In practice, it is found that for the conditions of these simulations, the variation of the velocity field at the inflow from the target values is small.

For the downstream boundary and the two sidewall boundaries, the nonreflecting boundary conditions of Thompson (1987, 1990) are used. The form of these conditions is allowed to switch between that for nonreflecting inflow and outflow at each point on the boundary depending on the instantaneous local normal velocity. This is particularly important for the outflow boundary across which large vortical structures are advected. Depending on the strength of the low speed stream, the sign of the longitudinal velocity can change across a structure. The two corner points on the outflow boundary are treated as nonreflecting at an angle 45 degrees from the two adjacent boundaries, and the two corner points on the inflow boundary are calculated using the characteristic inflow conditions.

It should be noted that these characteristic-based local boundary conditions were derived based on linearized waves propagating normal to the boundary, thus are not strictly non-reflecting in a multi-dimensional nonlinear flow. When the direction of wave propagation at the boundaries deviates from normal incidence, the amount of spurious reflection increases necessitating the use of filters for long-time stability of the turbulent jet simulations.

At all outflow points on the downstream and sidewall boundaries, the pressure correction term originally proposed by Rudy & Strikwerda (1980) and later discussed by Poinsot & Lele (1992) is

used,

$$\lambda_{in} n_i \frac{\partial W_{in}}{\partial x_i} = K \frac{p - p_\infty}{\rho c} \tag{18}$$

where,

$$K = \frac{\sigma c (1 - M_{max}^2)}{L} \tag{19}$$

In addition, a Perfectly Matched Layer, PML, buffer zone based on that of Hu (1996) was utilized on the downstream and sidewall boundaries in order to further isolate the interior of the domain from the effects of the boundary conditions. In this technique, a buffer region is added at the boundary where exponential damping terms are introduced into the governing equations of the form (written for the density equation on a boundary whose normal is in the x-direction),

$$\frac{\partial \rho}{\partial t} = \text{Standard Terms} - \sigma(x) \left(\rho - \overline{\rho} \right) \tag{20}$$

where,

$$\sigma(x) = \sigma_m \left(\frac{x - x^*}{L_b} \right)^\beta \tag{21}$$

In these expressions, x^* is the location of the interface between the buffer zone and the interior of the domain, $L_b = x_{max} - x^*$ is the length of the buffer zone, and we choose $\beta = 2.0$, $\sigma_m = 2.0$. This term acts to damp the density values to the specified mean value, $\overline{\rho}$, across the buffer zone. Similar terms are added in the the governing equations for pressure and momentum. On the sidewall boundaries, $j = 1$ and $j = j_{max}$, the longitudinal velocity is damped to the mean coflow velocity while on the outflow boundary the longitudinal velocity is damped to the profile of Bradbury (1965),

$$\frac{U - U_2}{\Delta U} = \exp \left[-0.6749 \eta^2 \left(1.0 + 0.027 \eta^4 \right) \right] \tag{22}$$

where $\eta = y / \delta_U$, with a target jet growth rate of $\delta_U / h = 0.1235 \left(x/h - 0.873 \right)$. The lateral velocity is damped to the profile given by the requirement that the mean velocity remain divergence free, $\partial U / \partial x + \partial V / \partial y = 0.0$. The value of the centerline velocity excess, $\Delta U = U_c - U_2$ in the outflow buffer zone is selected to maintain the same excess momentum flux

$$J = \rho \int_{-\infty}^{\infty} U \left(U - U_2 \right) dy \tag{23}$$

at the outflow plane as is present at the inflow. It was found through the course of this study that while damping to these "realistic" velocity profiles in a buffer region is required, it has a negligible impact on the flowfield in the region of interest. The pressure and density are damped to the constant initial values in the domain while the mean spanwise velocity is damped to zero. A grid stretching is also used in the buffer zones and is given by a simple geometric progression with a stretching ratio of 5%.

The longitudinal velocity in the shear layer on either side of the jet at the inflow is given by a hyperbolic tangent profile,

$$u = \frac{U_1 + U_2}{2} + \frac{\Delta U}{2} \tanh \left(\frac{y}{2\theta} \right) \tag{24}$$

where θ is the shear layer momentum thickness, U_1 and U_2 are the velocities of the high- and low-speed streams respectively and $\Delta U = U_1 - U_2$. This profile is mirrored about the jet centerline to

obtain a top-hat mean jet profile with smooth edges. The mean lateral and spanwise velocities are zero at the inflow. The mean pressure and density at the inflow are uniform initially, although a slight variation across the jet is generated due to the outgoing acoustic waves.

The mean profile for the passive scalar at the inflow is given by a hyperbolic tangent profile

$$\xi = \frac{\xi_1 + \xi_2}{2} + \frac{\xi_1 - \xi_2}{2} \tanh\left(\frac{y}{2\theta}\right) \tag{25}$$

with $\xi_1 = 1.0$ and $\xi_2 = 0.0$ in the jet and ambient, respectively. The value of θ used for the passive scalar is the same as that used for the mean longitudinal velocity profile.

A broadband inflow forcing is utilized with a three-dimensional energy spectra specified by

$$E(\kappa) = \frac{k^4}{16} \exp\left(-2(k/k_o)^2\right) \tag{26}$$

This forcing is designed to provide energy to the flowfield in a range of scales characteristic of that present in an actual turbulent flow in order to increase the rate at which the jet develops from the top-hat profile present at the inflow plane to the self-similar profiles downstream. This broadband forcing of the inflow plane is performed by generating a three-dimensional volume containing fluctuating velocity, pressure and density fields which is then convected past the inflow plane, as the simulation is integrated in time, using a constant convection velocity, U_c. Figure 1 shows the Reynolds stress profiles for the broadband fields used to force the inflow plane in the simulation discussed in § 4. The strong peaks in the shear layers on either side of the jet are clear, as well as the strong drop in intensity towards the jet centerline. The fluctuation intensity does not, however, decay completely at the jet centerline. The complete decay in the centerline intensity is incompatible with the requirement that the fluctuations be divergence free. While there are fluctuations present in the pressure and density at the inflow, their magnitude is small. The root-mean-square pressure fluctuations have a peak intensity of $p'_{rms}/\overline{\rho}\Delta U_o^2 = 1.1\times10^{-8}$ while the peak in the density fluctuations is $\rho'_{rms}/\overline{\rho} = 1.1\times10^{-9}$. Figure 2 shows the one-dimensional autospectra in the x- and z-directions of the longitudinal and spanwise components of velocity, respectively. The energy contained in these fluctuating fields is spread over a broad spectra in both time and the spanwise direction.

The computational grid used in this study was generated using a simple geometric progression, $\Delta y_{j+1} = A_j \Delta y_j$. Further details are provided later regard the specific grid used in each of the simulations.

4 Simulations of Three-Dimensional Turbulent Jets

This section discusses the evolution of a spatially evolving $Re_h = \rho\Delta U h/\mu = 3000$ jet with turbulent inflow. The Reynolds number based on the jet width increases to approximately 4700 at the outflow. The Schmidt number, $Sc = \mu/\rho D_\xi = 1.0$, and Prandtl number, $Pr = C_p\mu/k = 0.72$, for this simulation. The mean jet velocity at the inflow is given by equation 24 with a velocity ratio, $\eta = \Delta U/(U_1 + U_2) = 0.83$ while the convective Mach number, $M_c = \Delta U/(c_1 + c_2) = 0.16$. It is clear that, although this simulation is performed using the compressible Navier-Stokes equations, it is essentially incompressible. The momentum thickness for the shear layers at the inflow is $\theta/h = 0.05$. The inflow forcing for this jet has the spectrum, equation 26, while its intensity is $q/\Delta U = 0.10$ in the shear layers and $q/\Delta U = 1.9 \times 10^{-2}$ at the centerline of the jet, where $q^2 = \overline{u'u'} + \overline{v'v'} + \overline{w'w'}$. This simulation was performed on a $244 \times 221 \times 72$ computation grid with a physical domain size of $L_x/h = 13.5 + 1.5$, $L_y/h = 13.1 + 3.0$, $L_z/h = 4.0$ and a grid spacing in the domain interior of $\Delta x = \Delta y = \Delta z = 0.055h$. The designation, $L/h = a + b$, for the domain dimensions indicates that the interior of the domain has a size of a while there is a buffer zone of size b.

In the course of the discussion below, comparison of the current results against experimental data are made. The studies of Thomas & Chu (1989), Thomas & Prakash (1991) and Browne *et al.*

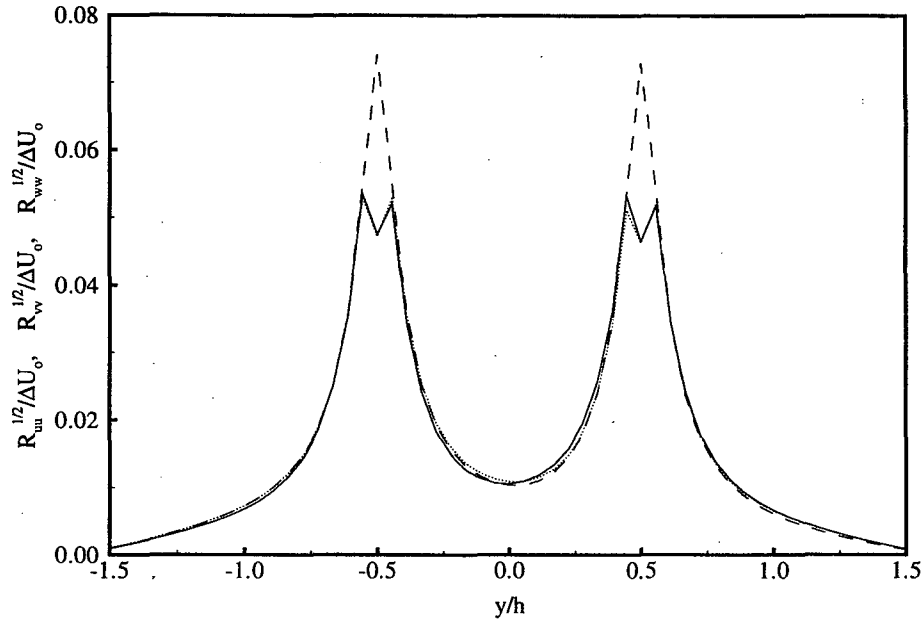

Figure 1: Reynolds stress profiles of the broadband fields utilized to force the three-dimensional jet simulations. —— $R_{uu}^{1/2}/\Delta U_o$, - - - $R_{vv}^{1/2}/\Delta U_o$, ····· $R_{ww}^{1/2}/\Delta U_o$

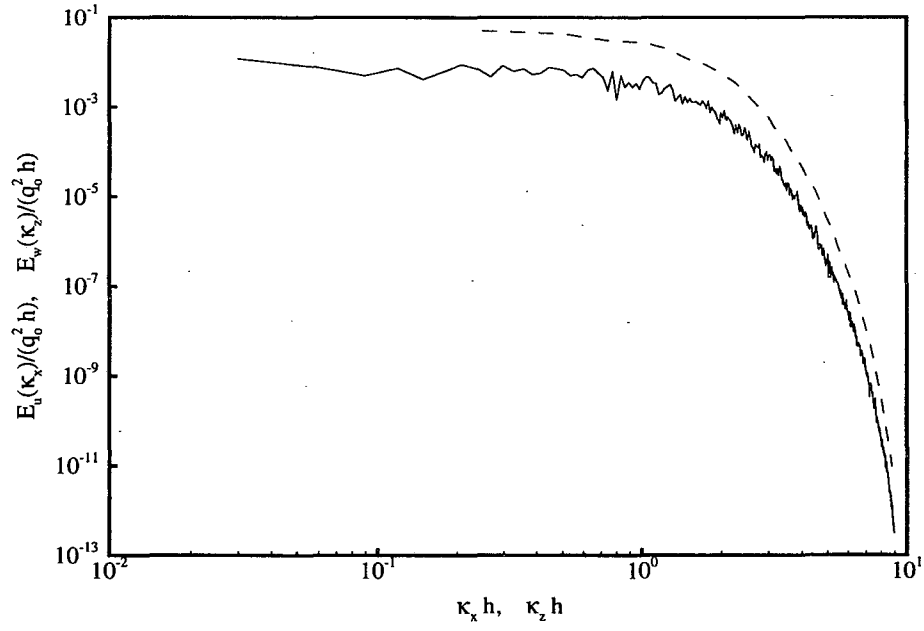

Figure 2: One-Dimensional autospectra in the x- and z-directions of the broadband velocity fields utilized to force the three-dimensional jet simulations. —— $E_u(\kappa_x)/(q_o^2 h)$, - - - $E_w(\kappa_z)/(q_o^2 h)$

Source	Re_h	h/θ	$[q/\Delta U]_{sl}$	$[q/\Delta U]_{cl}$
Ramaprian & Chandrasekhara (1985)	1,600	29*	-	-
Browne *et al.* (1983)	7,620	54	-	0.0035
Thomas & Prakash (1991)	8,000	67	-	≤ 0.0042
Thomas & Chu (1989)	8,300	67	-	≤ 0.0043
Gutmark & Wygnanski (1976)	30,000	-	-	0.0035
Hussain & Clark (1977)	32,550	182	0.071	0.021

Table 1: Physical parameters of the experimental results used for comparison. $*$ Momentum thickness, θ, estimated based on laminar flow in the nozzle.

(1983) are used for comparison of the downstream evolution of the jet width, centerline velocity decay, as well as centerline fluctuation intensities because they document the near field of the jet well. However, these studies do not provide complete measurements of the fully-developed region of the jet. The data in the fully-developed region of Gutmark & Wygnanski (1976) and Ramaprian & Chandrasekhara (1985) is used for evaluating the self-similar behavior. The physical conditions for these experimental studies are outlined in table 1 for comparison with the physical conditions of the current study.

Based on the spatially evolving linear stability analysis of the hyperbolic tangent velocity profiles performed by Michalke (1965) and the later work by Monkewitz & Huerre (1982) for different velocity ratios, $\eta = \Delta U/(U_1 + U_2)$, the fundamental frequency, f^*_{sl} (cycles per second), for the shear layer instability occurs at a Strouhal number of $S^*_{sl} = f^*_{sl}\theta/U_c = 0.033$ where θ is the momentum thickness of the shear layer and $U_c = (U_1 + U_2)/2$ is the convection velocity. The fundamental mode which is observed experimentally in the fully developed region of the jet is $S = f^*_{jt}\delta_U/\Delta U = 0.11$

For the nozzle conditions of the jet simulated here, the fundamental frequency for the shear layers at the jet nozzle is $f^*_{sl}\Delta U_o/h = 0.395$ while the peak frequency in the calculated energy spectrum at the outflow plane is $f^{pk}\Delta U_o/h = 0.07$.

4.1 Visualization of the Vorticity Field

Figure 3 shows instantaneous contours of the spanwise vorticity, ω_z, on an xy-plane through the domain at $z/h = 0.0$. It should be pointed out that the lateral extent of this plot, $y/h = \pm 4.0$, is not the full extent of the domain. The domain in this simulation has a lateral extent of approximately $13h$. In the region $0.0 \leq x/h \leq 4.0$ there is clear indication of the presence of vortex roll up in both the upper and lower shear layers. The spectral evolution along with the development of the shear layer instabilities will be investigated further in § 4.4. In the lower shear layer, peaks in the magnitude of the spanwise vorticity are present at $x/h = 3.5$ as well as $x/h = 2.0$ and a structure in the early stages appears to be present near $x/h = 0.5$. The streamwise wavelength of the spanwise vortices is consistent with the expected wavelength of the shear layer instability of $U_c/(f^*_{sl}h) = 1.52$.

Figure 4 shows an instantaneous xz-plane of the spanwise vorticity through the lower shear layer, $y/h = -0.53$. While there is some spanwise variation of ω_z in the shear layer for $0.0 \leq x/h \leq 2.0$, in general the structures appear to be relatively two-dimensional. The spanwise variations present in this region are small and of relatively long wavelength. However, downstream of $x/h = 2.0$ there is a rapid increase in the three-dimensionality of the structures present in the shear layer. This breakdown of the shear layer structures coincides with a strong growth in the magnitude of the streamwise vorticity, figure 5. Figure 5 shows contours of the streamwise vorticity, ω_x, on the xz-plane in the lower shear layer. While there is streamwise vorticity present in the shear layers at the inflow, only downstream of $x/h = 2.0$ is the magnitude of the streamwise vorticity consistent with that of the spanwise vorticity.

Figure 6 shows an xy-plane of the streamwise vorticity, ω_x, at the spanwise station, $z/h = 0.0$.

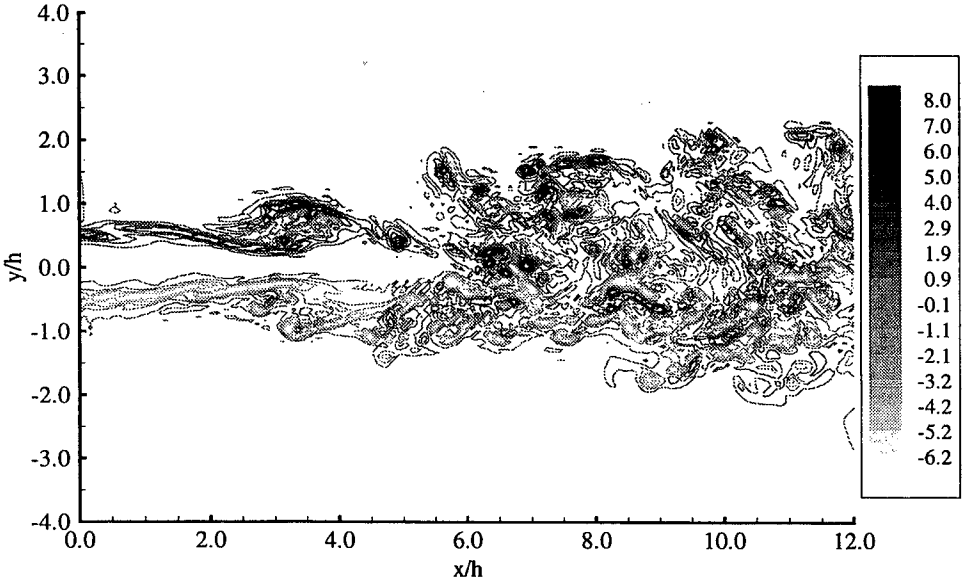

Figure 3: Instantaneous spanwise vorticity, ω_z, contours on an xy-plane located, $z/h = 0.0$.

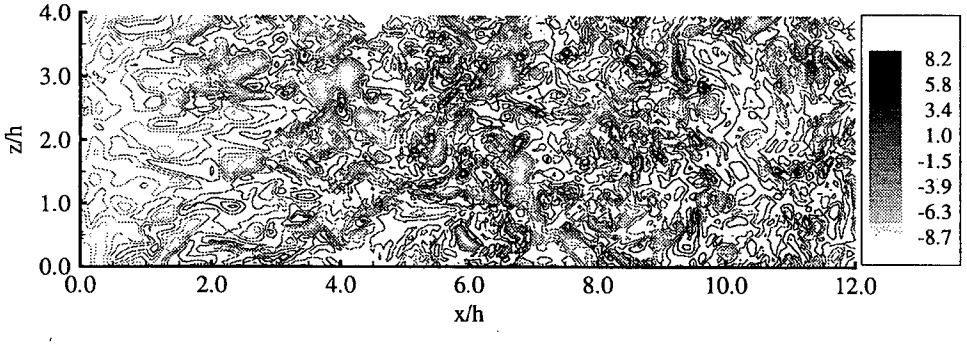

Figure 4: Instantaneous spanwise vorticity, ω_z, contours on an xz-plane in the lower shear layer, $y/h = -0.50$.

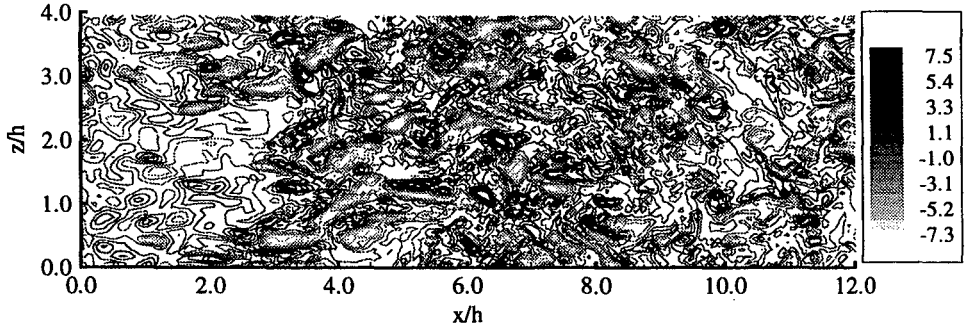

Figure 5: Instantaneous streamwise vorticity, ω_x, contours on an xz-plane in the lower shear layer, $y/h = -0.50$.

From figures 5 and 6 it is clear that the structures present in the streamwise vorticity for $2.0 \leq x/h \leq 4.0$ are elongated in the streamwise direction and have an inclination inwards towards the centerline of the jet suggesting stretching by the mean strain of the jet. The structure located in the lower shear layer of figure 6 for $2.5 \leq x/h \leq 3.0$ is located in the braid region between the two spanwise vortices at $x/h = 2.0$ and $x/h = 3.5$ which were noted in figure 3. The behavior of the structures in the spanwise and streamwise vorticity for $0.0 \leq x/h \leq 4.0$ is consistent with the roll up and pairing of spanwise vortices, generation of streamwise vortices, and eventual breakdown to strong three-dimensional turbulence which is observed in shear layers (for example Lasheras & Choi, 1988). It is clear that the beginning of the breakdown to strongly three-dimensional turbulence occurs before the merging of the shear layers for the jet simulated here.

The strong vorticity patches in the two shear layers near the inflow show signs of interacting in the region $4.0 \leq x/h \leq 6.0$. A few small patches of streamwise and spanwise vorticity begin to appear near the jet centerline in this range, figures 3 and 6. However, only downstream of $x/h = 6.0$ are there structures present in the vorticity field near the centerline of a magnitude similar to that present in the high shear region. In the downstream region of the jet, $x/h \geq 8.0$ the distribution of vorticity across the jet is relatively uniform from upper shear region across the centerline to the lower shear region. However, there are occasional regions devoid of strong vorticity near the jet edges, such as that along the upper edge of the jet near $x/h = 10.5$, due to the intermittent nature of the turbulence near the jet edges.

Figure 7 shows the downstream variation of the three root-mean-square vorticity components as well as the mean spanwise vorticity in the lower high shear region, $y/\delta_U \approx -1.0$. At the inflow of the jet, the RMS spanwise vorticity is a factor of four higher than the RMS streamwise or lateral vorticity. In the region $0.0 < x/h < 3.0$ the mean spanwise vorticity and the spanwise vorticity fluctuations decay while the streamwise and lateral vorticity fluctuations grow strongly. Downstream of $x/h = 2.5$ all three components of the root-mean-square vorticity are greater than the mean vorticity. This coincides with the rapid increase in three-dimensionality of the vorticity contours observed in figure 4.

The root-mean-square of the centerline fluctuating vorticity (not shown) does not begin to grow until $x/h \approx 4.0$ after which there is strong growth in the region $4.0 < x/h < 7.0$. The spanwise vorticity fluctuation intensity begins to grow slightly earlier than the streamwise and lateral components, although, the centerline values for the three components are generally of the same magnitude throughout the domain. While all three components of the RMS vorticity are of relatively the same magnitude on the jet centerline, in the high shear region the streamwise vorticity fluctuations are consistently larger than the spanwise and lateral components.

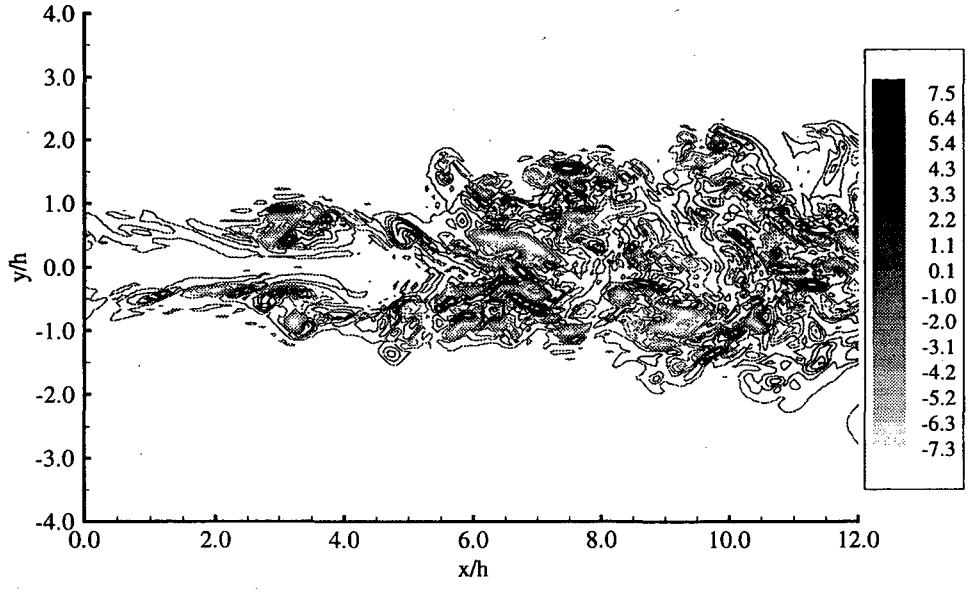

Figure 6: Instantaneous streamwise vorticity, ω_x, contours on an xy-plane, $z/h = 0.0$.

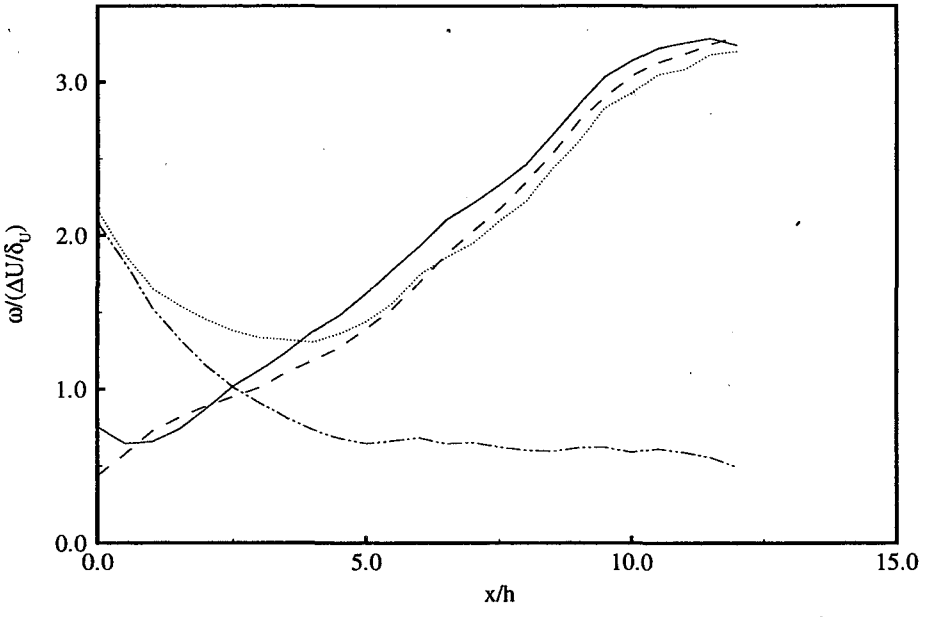

Figure 7: Downstream growth of the root-mean-square vorticity and mean spanwise vorticity in the lower high shear region, $y/\delta_U \approx -1.0$. —— $(\overline{\omega_x'^2})^{1/2}/(\Delta U/\delta_U)$, - - - $(\overline{\omega_y'^2})^{1/2}/(\Delta U/\delta_U)$, ····· $(\overline{\omega_z'^2})^{1/2}/(\Delta U/\delta_U)$, -·-·- $\overline{\omega_z}/(\Delta U/\delta_U)$

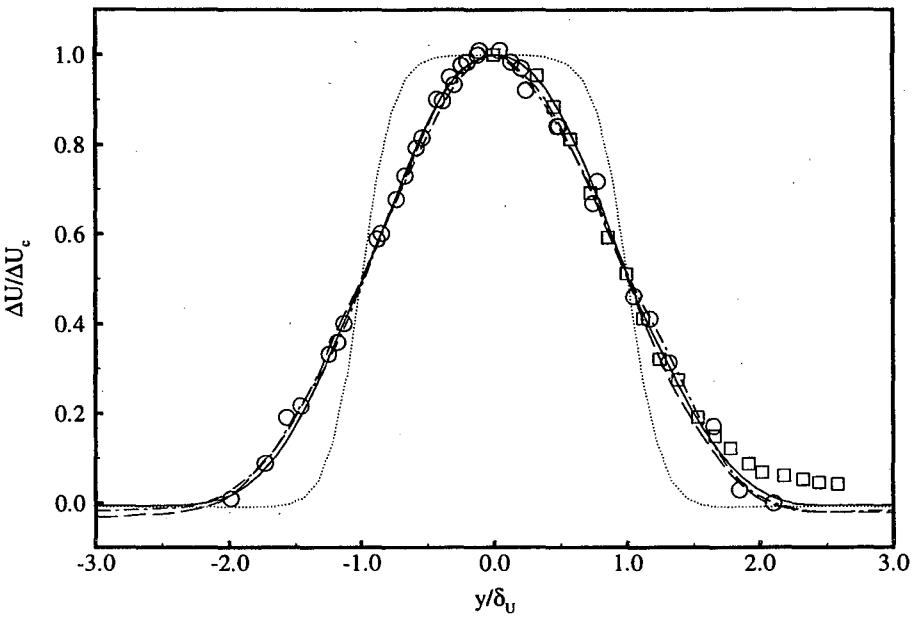

Figure 8: Mean longitudinal velocity profiles in a planar jet. ····· $x/h = 0.0$, —— $x/h = 4.0$, – – – $x/h = 8.0$, — — $x/h = 11.5$, □ Gutmark & Wygnanski (1976), ○ Ramaprian & Chandrasekhara (1985).

4.2 Mean Velocity

Figure 8 shows the mean streamwise velocity profiles at several downstream stations compared with experimental results from Gutmark & Wygnanski (1976) and Ramaprian & Chandrasekhara (1985). The mean profiles at $x/h = 0.0$ clearly shows the sharp shear layers on either side of the jet. The streamwise velocity profiles from the three downstream stations shown, $x/h \geq 4.0$, collapse to a self-similar profile which compares well with the experimental data.

Figure 9 shows the mean profiles of the lateral velocity component at three stations in the jet. In a jet, the free-stream value of the mean cross-stream velocity, V, is equivalent to the entrainment velocity, V_e. The most upstream station shown, $x/h = 5.0$, is the first station at which the entrainment velocity, V_e, has approached the magnitude of the self-similar value, $V_e/\Delta U_c \approx 0.035$. It can be seen that this value of the entrainment compares well with those of Gutmark & Wygnanski (1976) and Ramaprian & Chandrasekhara (1985). Although the mean lateral profiles do not collapse as well in the self-similar region as the mean longitudinal profiles, they compare well with experimental data.

Figure 10 shows the downstream growth in the jet half-width based on the longitudinal velocity. Following the plane jet similarity analysis, the width of the jet is expressed as the half-width, δ_U, defined as the distance from the jet centerline to the point at which the mean streamwise velocity excess, $U_e = U - U_2$, is half of the centerline velocity excess. In this definition U_2 is the local coflow velocity. Also shown in figure 10 is the experimental data from Thomas & Chu (1989) and Browne *et al.* (1983). It can be seen that the growth of the jet compares well with the experimental results in the initial developing region. Analysis of the self-similar region of planar jets predicts a linear relationship between the jet width and the streamwise coordinate, x,

$$\frac{\delta_U}{h} = K_{1u}\left[\frac{x}{h} + K_{2u}\right] \tag{27}$$

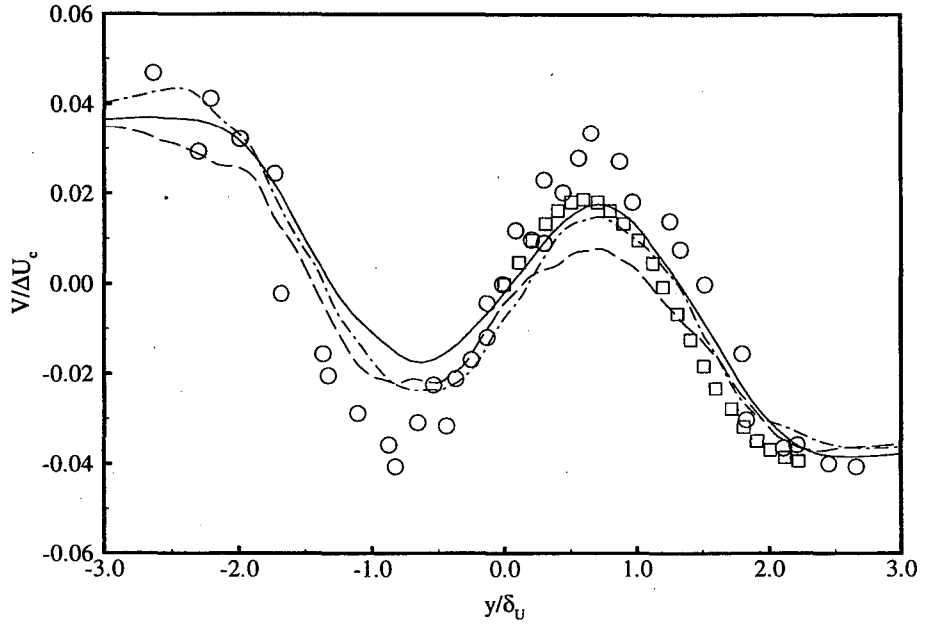

Figure 9: Mean lateral velocity profiles in a planar jet. —— $x/h = 5.0$, $-\cdot-$ $x/h = 10.5$, $--$ $x/h = 11.5$, □ Gutmark & Wygnanski (1976), ○ Ramaprian & Chandrasekhara (1985).

The current results give the values $K_{1u} = 0.093$ and $K_{2u} = 0.155$ for the linear growth region of the jet. These values are obtained using a linear fit of the current data in the region from $x/h = 6.0$ to 12.0. The linear growth rates are compared in table 2 with data from several experimental studies of planar jets. While the Reynolds number for these experimental studies vary, the self-similar growth rates are relatively consistent. The growth rates for the current results compare generally well with the experimental results, although they are approximately 10% lower. There is a large variation in the virtual origins K_{2u} of the experimental studies which makes a comparison difficult. Since the virtual origins of the plane jet are strongly affected by the conditions at the nozzle (see Stanley & Sarkar, 1999) it is expected that these values will vary.

Figure 11 shows the centerline velocity decay compared against the experimental data of Thomas & Chu (1989) and Browne *et al.* (1983). It can be seen that the centerline velocity decay for this simulation compares well with the experimental results. The analysis of planar jets predicts an inverse-squared relationship between the mean centerline velocity excess and the downstream

Source	K_{1u}	K_{2u}	C_{1u}	C_{2u}
DNS results, $q/\Delta U_o = 0.10$	0.093	0.155	0.193	0.128
Ramaprian & Chandrasekhara (1985)	0.110	-1.00	0.093	-1.60
Browne *et al.* (1983)	0.104	-5.00	0.143	-9.00
Thomas & Prakash (1991)	0.110	0.140	0.220	-1.20
Thomas & Chu (1989)	0.110	0.140	0.220	-1.19
Gutmark & Wygnanski (1976)	0.100	-2.00	0.189	-4.72
Hussain & Clark (1977)	0.118	2.15	0.123	4.47

Table 2: Jet growth rates and centerline velocity decay rates for the current results and several experimental studies.

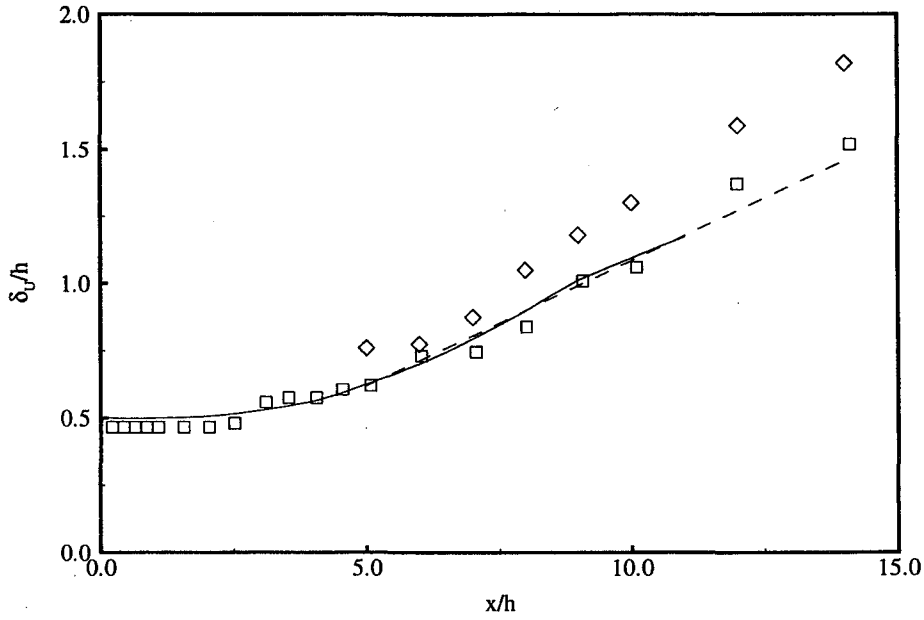

Figure 10: Downstream growth of the jet half-width based on velocity. —— Current results, - - - $\delta_U/h = 0.093(x/h + 0.155)$, □ Thomas & Chu (1989), ◇ Browne *et al.* (1983).

coordinate, x,

$$\left(\frac{\Delta U_o}{\Delta U_c}\right)^2 = C_{1u}\left[\frac{x}{h} + C_{2u}\right] \tag{28}$$

where ΔU_o is the centerline mean velocity excess at the jet nozzle and ΔU_c is the centerline mean velocity excess at the specific x/h station. The current results predict values for the coefficients, $C_{1u} = 0.193$ and $C_{2u} = 0.128$. Table 2 shows a comparison of these values with results from several experimental studies. It is clear that there is a broad variation in the values of the centerline velocity decay rate as well as the virtual origins between the different studies. However, the current results are well within the range of values from the experimental data. Based on the constancy of the centerline mean longitudinal velocity the length of the potential core of this jet is approximately $l_p/h = 4.0$. This compares well with the range observed experimentally of 2.5 to 5.0 for jets with Reynolds numbers ranging from 1000 to 7000 (Thomas & Chu, 1989; Browne *et al.*, 1983; Namer & Ötügen, 1988).

The turbulent planar jet is a flow in which the mean Reynolds number, $Re_{\delta_U} = 2\rho\delta_U\Delta U_c/\mu$, grows downstream in the self-similar region as $Re_{\delta_U} \propto x^{1/2}$. In the current simulation the mean Reynolds number remains nearly constant at the inflow Reynolds number of $Re_h = 3000$ up to $x/h = 3.0$. However, downstream of $x/h = 3.0$, the mean Reynolds number grows strongly with the expected variation of $x^{1/2}$. At $x/h = 12.0$, the mean Reynolds number has grown to a value of $Re_{\delta_U} = 4692$.

A planar jet issuing into a coflowing stream does not strictly follow the self-similar behavior discussed above. The addition of the coflow is not a pure Galilean transformation in that it imposes a relative velocity between the jet nozzle and the coflowing stream. Planar jets in a coflowing stream have been studied experimentally by Bradbury (1965), Bradbury & Riley (1967), Everitt & Robins (1978) and LaRue *et al.* (1997) as well as computationally by Reichert & Biringen (1997) and Stanley & Sarkar (1997*a*,*b*). A plane jet exhausting into a stagnant fluid will develop from the nozzle until

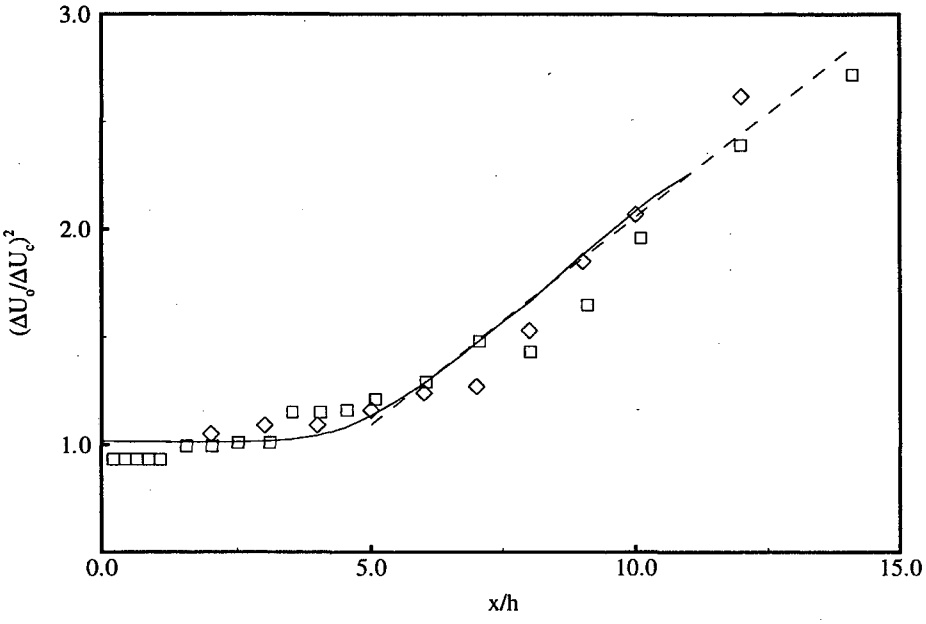

Figure 11: Decay of the mean velocity excess on the jet centerline. ——Current results, - - -$(\Delta U_o/\Delta U_c)^2 = 0.193(x/h + 0.128)$, □ Thomas & Chu (1989), ◇ Browne *et al.* (1983).

it exhibits the self-similar behavior discussed above, $\delta_U \propto x$ and $U_c \propto x^{-1/2}$ and continue to do so. A jet exhausting into a coflowing stream, on the other hand, will initially develop the self-similar behavior characteristic of a plane jet into stagnant fluid. However, when the ratio of centerline velocity to coflow velocity, U_c/U_2, approaches unity it will transition into a self-preserving wake-like behavior with $\delta_U \propto x^{1/2}$ and $\Delta U_c \propto x^{-1/2}$ (Bradbury, 1965; Bradbury & Riley, 1967). For the initial velocity ratio used in this study, $U_j/U_2 = 11$, it is clear from figure 10 that self-preserving jet-like behavior is observed. Bradbury & Riley (1967) observed a region of linear growth characteristic of jet-like behavior with jets having an initial velocity ratio of $\Delta U_o/U_2 = 6.25$ as did LaRue *et al.* (1997) for $\Delta U_o/U_2 = 5$. However, in both of these cases the jet growth rate, K_{1u}, was on the order of ≈ 0.02, or a factor of five below the rate observed for jets exhausting into stagnant fluid. From the good comparison of the linear jet growth rates in the current study with the observed data for jets exhausting into stagnant fluid it is clear that the small coflow velocity in this study has a minimal effect on the development of the jet. However, the nonzero coflow velocity could account for the fact that the growth rates in our jet are slightly low compared to experiments.

4.3 Reynolds Stresses

Figures 12, 13, and 14 show the downstream evolution of the Reynolds stresses R_{uu}, R_{vv}, and R_{ww}, respectively, on the jet centerline compared to the experimental data of Thomas & Chu (1989), Thomas & Prakash (1991) and Browne *et al.* (1983). It can be seen from these figures that the length of the potential core, based on the location of strong growth of the centerline fluctuations, is approximately $2 - 3$ jet widths and is consistent with the experimentally observed values. In the current results, the fluctuation intensities on the jet centerline grow strongly in the region $2.0 < x/h < 12.0$. While the longitudinal and spanwise centerline intensities appear to asymptote to their self-similar values by $x/h = 12.0$, the lateral intensities still show a slight growth at the most

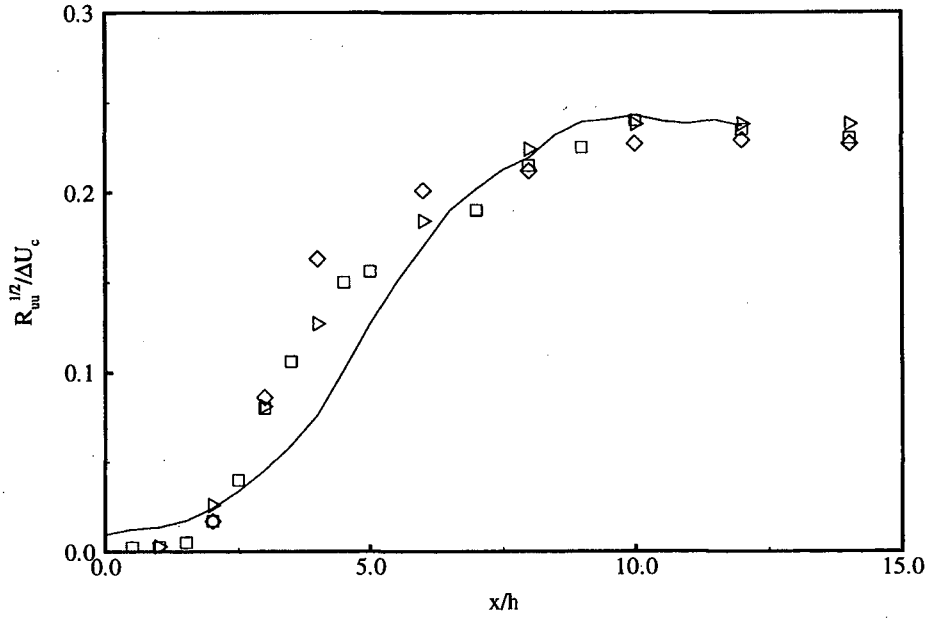

Figure 12: Growth of the longitudinal Reynolds stress on the jet centerline. —— Current results, □ Thomas & Chu (1989), ▷ Thomas & Prakash (1991), ◇ Browne *et al.* (1983).

downstream station.

It should be noted that the initial fluctuation intensities in the shear layers of the DNS case discussed here are relatively high. The typical approach in experimental studies is to report the fluctuation intensity at the centerline of the nozzle, rather than in the shear layers. Since the fluctuation intensities peak in the boundary layers on the nozzle lips, the centerline intensity is not sufficient to quantify the inflow conditions of the jet. In the studies of Thomas and Chu, Thomas and Prakash as well as Browne *et al.* the centerline fluctuation intensity is on the order of 0.35%, table 1. However, the peak intensity in the shear layers from these studies is unknown. Likewise, the spectral content of the inflow fluctuations from these experiments is unknown. The centerline fluctuation intensity for the current study is 1.9% while the peak intensity in the shear layers is $\approx 10\%$ of the jet nozzle velocity.

The initial rate of growth of the fluctuations at the jet centerline is consistent with the experimental studies, although the initial growth rate of the longitudinal fluctuation intensity in the region $2.0 < x/h < 5.0$ is a little low, figure 12. As discussed in Stanley & Sarkar (1999), the initial growth of turbulence intensities is weaker for thicker shear layers and therefore the slower growth in the simulation may be related to the smaller $h/\theta = 20$ in the DNS relative to experimental values, see table 1. In the experiments, the longitudinal fluctuations grow more rapidly near the inflow than the lateral or spanwise components. In the current results all three components of the fluctuating velocity field grow at approximately the same rate on the jet centerline. This difference is likely due to the difference in the inflow fluctuation intensities between the current study and the experimental results. In shear flows, the longitudinal fluctuation intensities grow due to the production by the mean shear before the transfer of energy to the lateral and spanwise components can occur. The redistribution of energy is larger in nonlinearly evolving turbulent flows than in transitional or rapidly-distorted flows. Therefore the transfer of energy from the longitudinal component to the lateral and spanwise components occurs more rapidly in the DNS where there is initially energy in all three velocity components at a level which is larger than that in experiments.

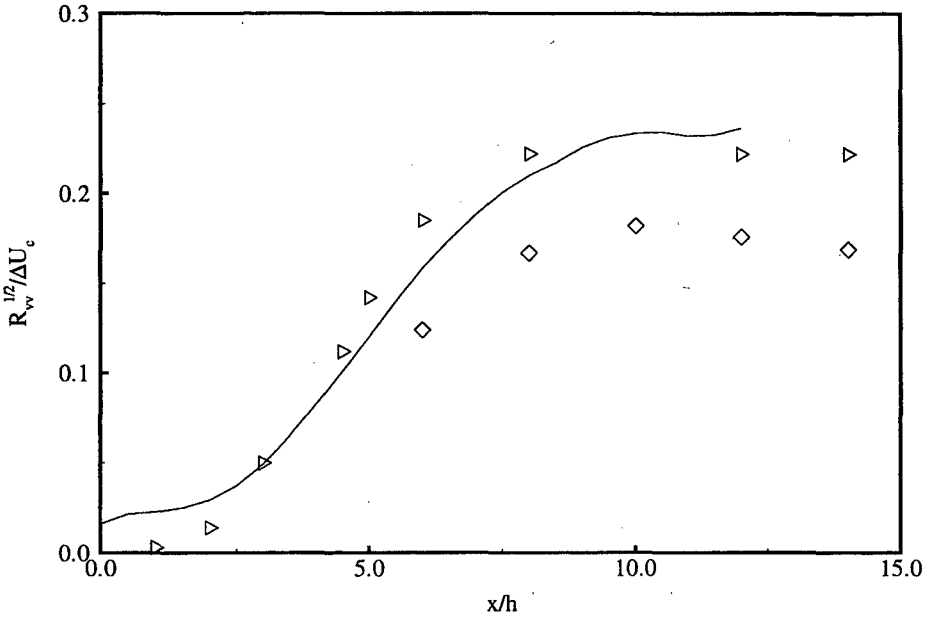

Figure 13: Growth of the lateral Reynolds stress on the jet centerline. —— Current results, ▷ Thomas & Prakash (1991), ◇ Browne *et al.* (1983).

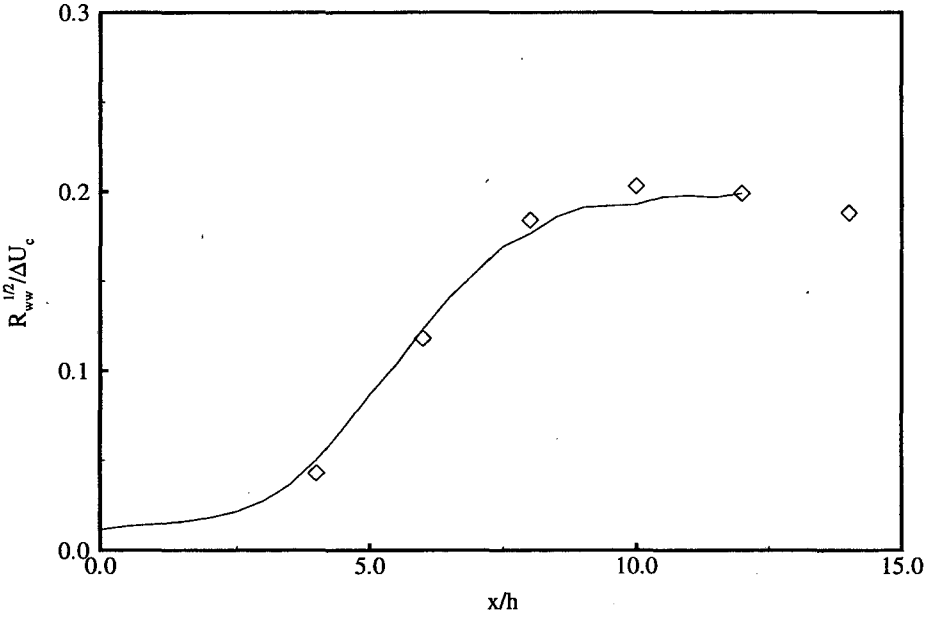

Figure 14: Growth of the spanwise Reynolds stress on the jet centerline. —— Current results, ◇ Browne *et al.* (1983).

Source	$\overline{u'u'}/\overline{q^2}$	$\overline{v'v'}/\overline{q^2}$	$\overline{w'w'}/\overline{q^2}$	$\lvert\overline{u'v'}\rvert/\overline{q^2}$
DNS Results, Lower S.L.	0.52	0.22	0.27	0.19
Upper S.L.	0.48	0.22	0.30	0.19
Wygnanski & Fiedler (1970)	0.43	0.26	0.31	0.13
Spencer & Jones (1971)	0.53	0.23	0.23	0.20
Bell & Mehta (1990)	0.44	0.27	0.29	0.14

Table 3: Comparison of the shear layer turbulence intensities at $x/h = 4.0$ with experimentally measured values for turbulent shear layers.

The direct production of energy by the mean shear into the R_{uu} component in the sharp shear layers, $y/\delta_U = \pm 1.0$, for $x/h \leq 2.0$ leads to a strong anisotropy in the fluctuating fields in this region of the jet. At the station $x/h = 2.0$, the longitudinal component is more than six times the lateral component and more than three times the spanwise component leading to anisotropy in the normal components which is far greater than is present in the fully developed region of turbulent shear layers. However the shear component of the anisotropy $\overline{u'v'}/\overline{q^2} = \pm 0.17$ agrees quite well with experimentally measured values in turbulent shear layers.

In the region $2.0 \leq x/h \leq 4.0$ the anisotropy in the shear layers relaxes to values which are more characteristic of those present in turbulent shear layers. Table 3 shows a comparison of the anisotropy values in the shear layers at the station $x/h = 4.0$ from the current results against the experimental values from Wygnanski & Fiedler (1970), Spencer & Jones (1971) as well as Bell & Mehta (1990) for fully developed turbulent shear layers. By this station, the shear layer Reynolds stresses have reached levels of anisotropy which are comparable to those present in turbulent shear layers. There is still an imbalance between the lateral and spanwise components; however, they have both become more comparable with the longitudinal component of the Reynolds stress. The ordering of the intensities is as would be expected, for a turbulent shear flow with the mean shear in the y-direction, with $\overline{u'u'}/\overline{q^2} > \overline{w'w'}/\overline{q^2} > \overline{v'v'}/\overline{q^2}$. The Reynolds shear stress, as mentioned above, compares well with the values from turbulent shear layers even earlier in the jet.

Figures 15, 16 and 17 show the profiles of the three normal Reynolds stress components downstream in the jet near the outflow of the domain. Shown in these figures are two stations from the current simulation, and experimental data from Gutmark & Wygnanski (1976) and Ramaprian & Chandrasekhara (1985). From the two stations shown, $x/h = 10.0$ and 11.5, it can be seen that the Reynolds stress components are very close to self-similarity near the outflow of the domain. The comparison of the current results against the experimental data is good. The longitudinal fluctuation intensities, figure 15, fall within the range of experimental data. The current results show the strong dip at the centerline in the longitudinal Reynolds stress, R_{uu}, which is characteristic of planar jets and results from the fact that the regions of strong production are in the shear layers on either side while the production is small near the centerline. While the spanwise intensities match the experimental data well, the lateral intensities are somewhat high. In most experimental studies self-similarity of the Reynolds stress profiles is reached only after 30 to 40 jet widths downstream. By design, the relatively high intensity fluctuations at the inflow are chosen here to allow a more rapid transition from the developing region to a self-similar state. The shear stress profiles (not shown here) also compare well with experimental data.

Figure 18 shows the balance of the terms in the turbulent-kinetic-energy equation in the self-similar region of the jet. The trace of the pressure-strain term, $\Pi^*/\overline{\rho}$, also called the pressure-dilatation is insignificant. The strong production, P^*, of turbulent energy in the regions of peak shear, $y/\delta_U \approx \pm 0.8$, as well as the more uniform strong viscous dissipation of energy, $-\epsilon^*$, can be seen in the core of the jet, $-1 \leq y/\delta_U \leq 1$. The advection term in the turbulent-kinetic-energy equation acts to transport energy from the edges of the jet in towards the centerline while the turbulent transport term, $-\partial_j T_j^*/\overline{\rho}$, acts to transport fluctuating energy away from the region of

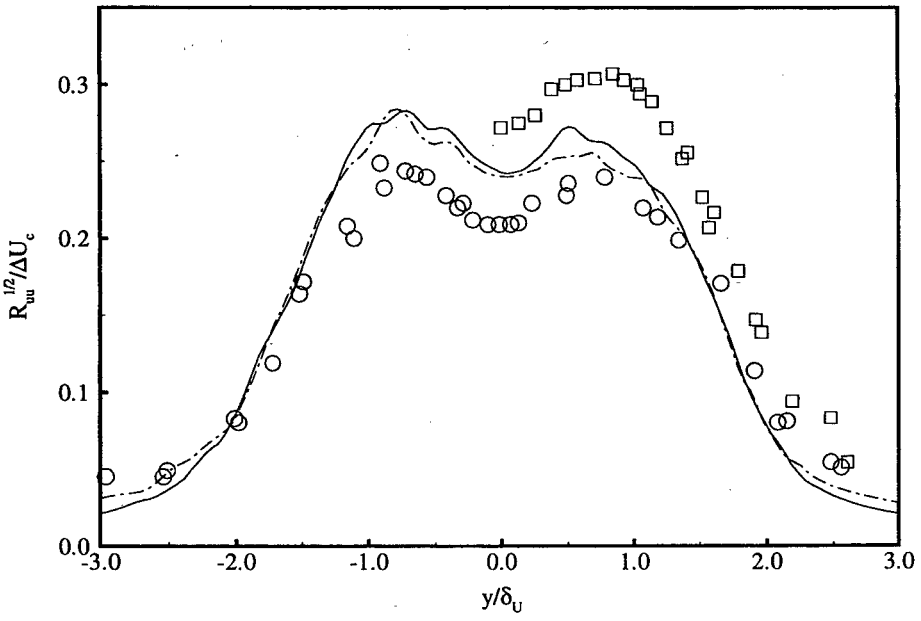

Figure 15: Longitudinal Reynolds stress profiles downstream in the jet. —— $x/h = 10.0$, – – – $x/h = 11.5$, □ Gutmark & Wygnanski (1976), ○ Ramaprian & Chandrasekhara (1985).

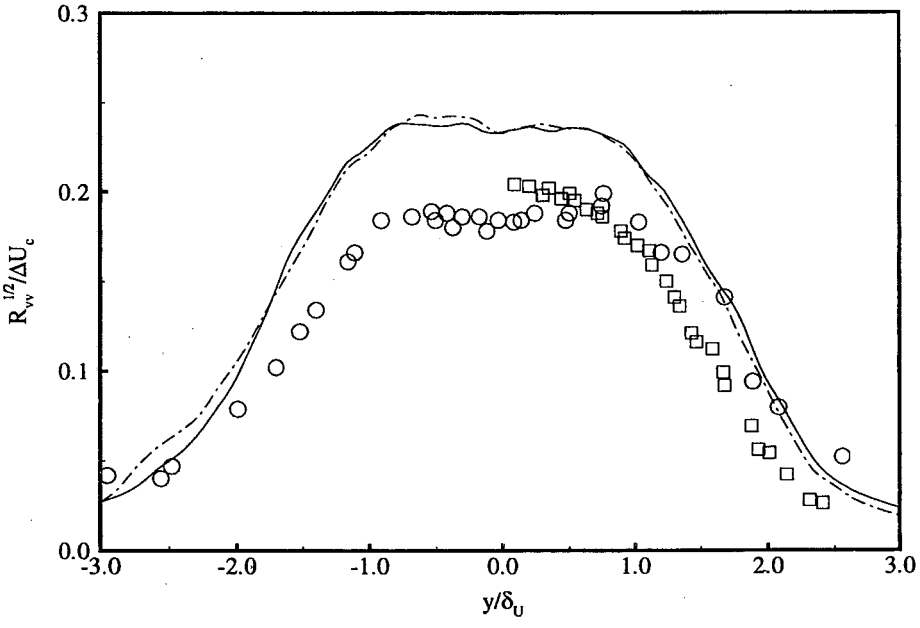

Figure 16: Lateral Reynolds stress profiles downstream in the jet. —— $x/h = 10.0$, – – – $x/h = 11.5$, □ Gutmark & Wygnanski (1976), ○ Ramaprian & Chandrasekhara (1985).

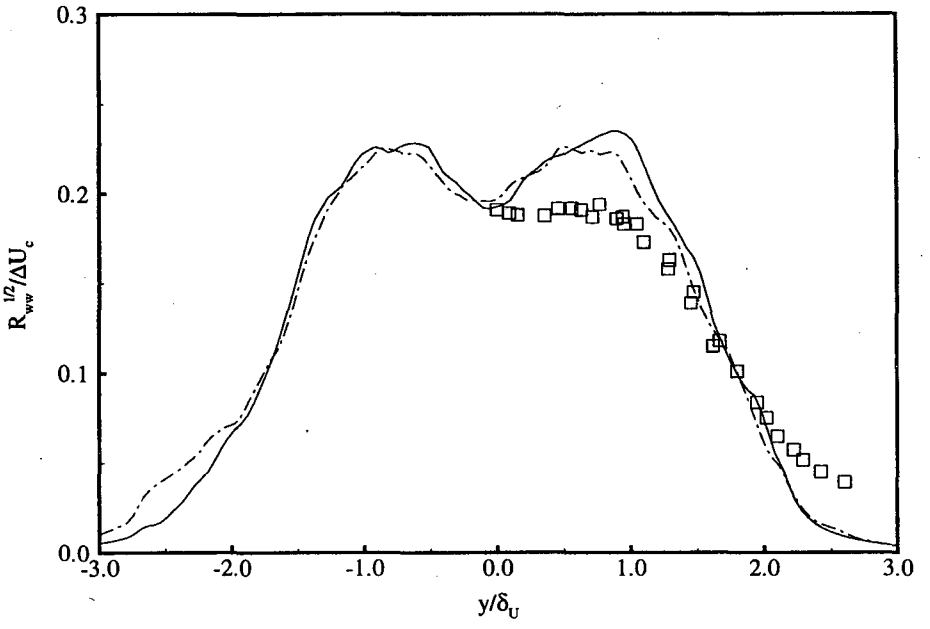

Figure 17: Spanwise Reynolds stress profiles downstream in the jet. —— $x/h = 10.0$, – – – $x/h = 11.5$, □ Gutmark & Wygnanski (1976).

peak production towards the jet centerline as well as the jet edges. It is clear by the fact that the production term is zero at the jet centerline that the action of the advection and turbulent transport terms are the sole means by which fluctuating energy is present at the core of the jet.

Near the outer edges of the jet, as discussed by Tennekes & Lumley (1972), the balance is predominately between the turbulent transport term and the advection. At this point in the jet, the turbulent transport term acts to spread turbulent energy outwards towards the jet edges while the advection due to the entrainment velocity, V_e, propagates energy inwards. It is the balance between these two terms which results in the edge of the turbulent jet being stationary in the mean.

In general, the turbulent-energy balance for the current results compares well with the energy balances shown by both Ramaprian & Chandrasekhara (1985) as well as Gutmark & Wygnanski (1976). However, a strong advantage of the current results in the study of the energy balance is that every term in the balance can be calculated. In experimental studies in the past, it has been necessary to make various approximations regarding the terms in the turbulent-kinetic-energy equation in order to estimate the balance of terms. Ramaprian and Chandrasekhara did not measure the spanwise velocity component, therefore they were forced to use an estimate of the turbulent kinetic energy based on the lateral and streamwise velocities only. Also, rather than measuring the dissipation directly, they estimated dissipation using the energy spectra of u'^2. Gutmark and Wygnanski, on the other hand, estimated the dissipation using the isotropic assumption, $\epsilon = 15\nu\overline{(\partial u'/\partial x)^2}$. In general, all of the studies have restricted the form of the turbulent-kinetic-energy equation using the boundary-layer approximation for the mean velocity profiles to drop terms. While it is recognized that these are likely good and necessary approximations, in some cases the higher-order effects may be significant. For instance, in the current study the isotropic approximation underestimates the dissipation by approximately 18% at the centerline of the jet.

The Reynolds stress anisotropy levels for $y/\delta_U = \pm 1.0$ in the self-similar region of the jet are shown in table 4 compared against available experimental data. The results from this DNS show greater isotropy of the normal stress components than the experimental data of Ramaprian & Chan-

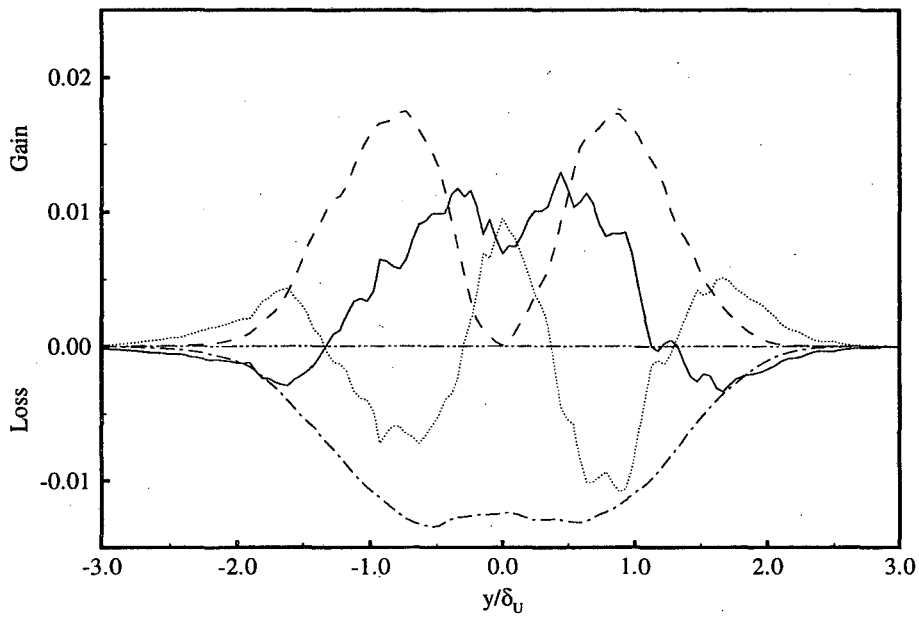

Figure 18: Balance of the terms in the turbulent kinetic energy equation in the self-similar region of the jet. —— Advection, - - - P^*, -·-·- $-\epsilon^*$, ····· $-\partial_j T_j^*/\overline{\rho}$, -··-·- $\Pi^*/\overline{\rho}$

Source	$\overline{u'u'}/\overline{q^2}$	$\overline{v'v'}/\overline{q^2}$	$\overline{w'w'}/\overline{q^2}$	$\lvert\overline{u'v'}\rvert/\overline{q^2}$
DNS Results, $y/\delta_U = 1.0$	0.386	0.311	0.310	0.148
$y/\delta_U = -1.0$	0.418	0.300	0.278	0.143
Gutmark & Wygnanski (1976)	0.591	0.191	0.218	0.143
Ramaprian & Chandrasekhara (1985), $y/\delta_U = 1.0$	0.397*	0.269*	-	0.152*
$y/\delta_U = -1.0$	0.423*	0.244*	-	0.145*

Table 4: Comparison of the jet turbulence intensities for $y/\delta_U = \pm 1.0$ in the self-similar region with experimentally measured values. * assumes $\overline{q^2} = 3/2(\overline{u'^2} + \overline{v'^2})$

drasekhara (1985) and Gutmark & Wygnanski (1976). The magnitudes of $\overline{v'v'}/\overline{q^2}$ and $\overline{w'w'}/\overline{q^2}$ are much more balanced in the self-similar region of the jet than was the case in the shear layers near the inflow. In both the DNS and experimental data the shear component of the isotropy, $\overline{u'v'}/\overline{q^2}$, is at a level consistent with those observed in turbulent shear layers, table 3. It should be noted that a strong asymmetry is present in the Reynolds shear stress profiles shown by Ramaprian & Chandrasekhara. Their peak values for R_{uv} are similar from side to side, however in the lower half-jet the peak occurs at $y/\delta_U = -1.0$ while their peak occurs at $y/\delta_U = 0.5$ in the upper half-jet. This explains the asymmetry in the shear component of the isotropy for their results.

At the jet centerline, table 5, the large-scale isotropy does not change drastically from the levels present in the high-shear region. The longitudinal component is smaller due to the lack of a strong mean gradient driving this component at the centerline, however, the change is not large. The lateral component is higher than the isotropic level of 1/3 while the spanwise component is below this level. It is clear that the large scales have not relaxed to isotropy in spite of the absence of mean shear at the centerline. This is consistent with the experimental data shown in the table although, as in the high-shear region, there is a large variation in the turbulence levels with Gutmark & Wygnanski

Source	$\overline{u'u'}/\overline{q^2}$	$\overline{v'v'}/\overline{q^2}$	$\overline{w'w'}/\overline{q^2}$
DNS Results	0.378	0.363	0.259
Gutmark & Wygnanski (1976)	0.485	0.275	0.240
Browne *et al.* (1983)	0.471	0.237	0.292
Ramaprian & Chandrasekhara (1985)	0.375*	0.289*	-
Everitt & Robins (1978)	0.385	0.338	0.277

Table 5: Comparison of the jet turbulence intensities on the centerline in the self-similar region with experimentally measured values. * assumes $\overline{q^2} = 3/2(\overline{u'^2} + \overline{v'^2})$

	$\frac{\overline{(\partial v'/\partial y)^2}}{(\partial u'/\partial x)^2}$	$\frac{\overline{(\partial w'/\partial z)^2}}{(\partial u'/\partial x)^2}$	$\frac{\overline{(\partial u'/\partial y)^2}}{(\partial u'/\partial x)^2}$	$\frac{\overline{(\partial u'/\partial z)^2}}{(\partial u'/\partial x)^2}$	$\frac{\overline{(\partial v'/\partial x)^2}}{(\partial v'/\partial y)^2}$	$\frac{\overline{(\partial v'/\partial z)^2}}{(\partial v'/\partial y)^2}$	$\frac{\overline{(\partial w'/\partial x)^2}}{(\partial w'/\partial z)^2}$	$\frac{\overline{(\partial w'/\partial y)^2}}{(\partial w'/\partial z)^2}$
Isotropic Values	1.0	1.0	2.0	2.0	2.0	2.0	2.0	2.0
$y/\delta_U = 1.0$	1.11	1.27	2.36	2.31	1.57	2.02	1.58	2.09
$y/\delta_U = -1.0$	1.17	1.28	2.36	2.35	1.46	1.99	1.53	2.11
Centerline	0.94	1.01	1.98	2.03	1.87	1.85	1.89	1.83

Table 6: Derivative variances in the self-similar region of the jet.

having the highest levels and Ramaprian & Chandrasekhara as well as Everitt & Robins having more isotropic values consistent with the DNS results.

While it is clear that the large scales of the flow adjust slowly to isotropy in the absence of mean shear at the centerline, the small scales adjust quite rapidly. Table 6 lists the velocity derivative variances for the centerline as well as the upper and lower high-shear regions in the self-similar region of the jet near the outflow. In the high shear regions, above and below the centerline, the deviation with respect to the isotropic condition that $\overline{(\partial u'/\partial x)^2} = \overline{(\partial v'/\partial y)^2} = \overline{(\partial w'/\partial z)^2}$ is as large as 28% while at the centerline of the jet this condition is met to within 6%. To a close approximation the cross derivatives variances of the longitudinal velocity, $\overline{(\partial u'/\partial y)^2}$ and $\overline{(\partial u'/\partial z)^2}$, are very nearly equal at both the centerline as well as in the shear region. Although significantly different from the isotropic estimate in the shear regions, the ratio of these terms to the normal derivative variance, $\overline{(\partial u'/\partial x)^2}$, approaches the isotropic value of 2.0 near the centerline. The cross derivative variances of the lateral and spanwise velocity components are more affected by the mean shear than those of the longitudinal velocity, so that $\overline{(\partial v'/\partial x)^2} \neq \overline{(\partial v'/\partial z)^2}$ and $\overline{(\partial w'/\partial x)^2} \neq \overline{(\partial w'/\partial y)^2}$ in the regions of strong shear. However, near the centerline these conditions are met quite well and the ratios of these cross-derivative variances to their respective normal-derivative variances match the isotropic values to within 9%. It is clear from this data that the small scales of motion in the self-similar region of the jet adjust rapidly, in space, to the local mean velocity profile so that near the centerline of the jet the small scales are, to a relatively good approximation, isotropic. However, as mentioned previously, the isotropic approximation for the dissipation underestimates the centerline dissipation by approximately 18% because of the accumulation of errors in the individual components that are summed to give the dissipation rate, ϵ.

4.4 Spectral Evolution

Figure 19 shows the longitudinal velocity autospectra in time near the nozzle in the upper shear layer, $y/\delta_U = 1.0$. The frequency and power spectral density in this plot are scaled using conditions in the shear layer at the inflow. As mentioned earlier, the most unstable mode in the shear layer occurs at a Strouhal number, $S = f\theta/U_c = 0.033$. It is clear from figure 19 that the initial growth of the fluctuations in this simulation is dominated by the interaction of the relatively high intensity

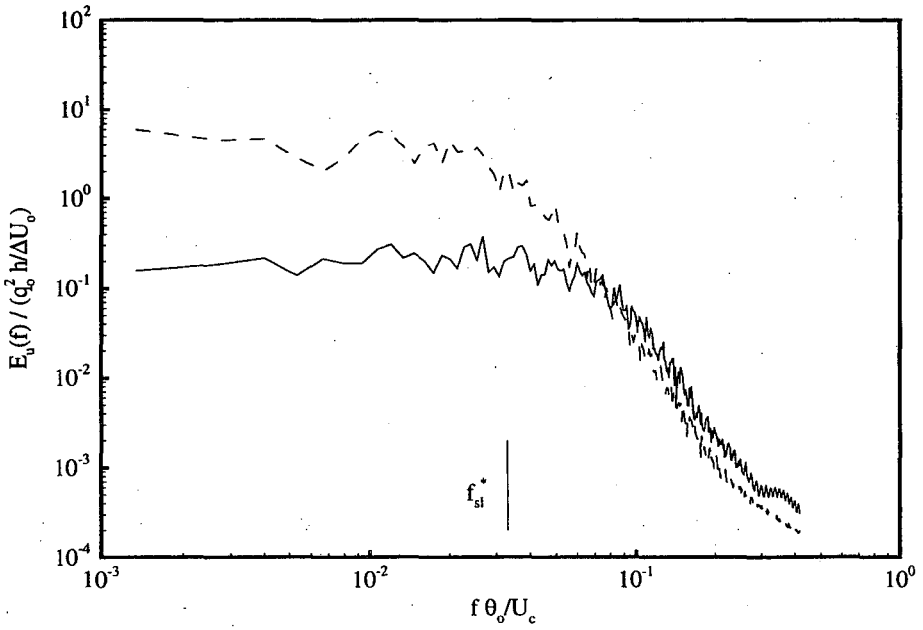

Figure 19: One-dimensional autospectra in time of the longitudinal velocity in the upper shear layer. —— $x/h = 0.0$, - - - $x/h = 1.0$.

fluctuations at the inflow with the mean shear, as opposed to the linear instability associated with the shear layer. While the shear layer mode does indeed grow, the strongest increase in energy in the autospectra occurs at larger scales where the energy due to the effects of mean shear is introduced into the fluctuating fields. Unlike the results for the two-dimensional forced jets of Stanley & Sarkar (1997*b*), discrete peaks at f_{sl}^* and its subharmonics do not develop. It is also interesting to note that there is a decrease in the energy at the intermediate and small scales, $S \geq 0.05$, relative to the energy in the large-scales. As the turbulent cascade develops downstream the energy in the intermediate and small scales grows strongly.

The absence of a strong peak in the autospectra coincident with the shear layer mode near the nozzle is a result of the strong broadband inflow forcing. The energy of the shear layer mode is not significantly greater than the broadband background energy, and thus is not visible in the autospectra. However, the vorticity visualizations of § 4.1 show distinct spanwise vortices and their interaction. In order to reduce the influence of the broadband background energy and accentuate discrete frequencies, coherency spectra that use information at two separate locations in the flowfield are obtained. Figure 20 shows the coherency spectra of the lateral velocity at two points in the shear layers on opposite sides of the jet, $y/\delta_U = \pm 1.0$. The coherency spectra of a variable A is defined as

$$\mathrm{Coh}_{12}(f,\Delta) = |E_{12}(f,\Delta)| = \left| \int_{-\infty}^{\infty} C_{12}(\tau,\Delta) \exp\left(-2\pi i f \tau\right)\, d\tau \right| \tag{29}$$

where

$$C_{12}(\tau,\Delta) = \lim_{T\to\infty} \frac{1}{T A_1^{rms} A_2^{rms}} \int_0^T A_1(t) A_2(t+\tau)\, dt \tag{30}$$

is the correlation coefficient in time between the values of A at two points separated by a distance Δ. In this definition, A^{rms} indicates the root-mean-square value of the time series A and $E_{12}(f,\Delta)$ is the Fourier transform of the correlation coefficient $C_{12}(\tau,\Delta)$. The spectra in figure 20 are normalized

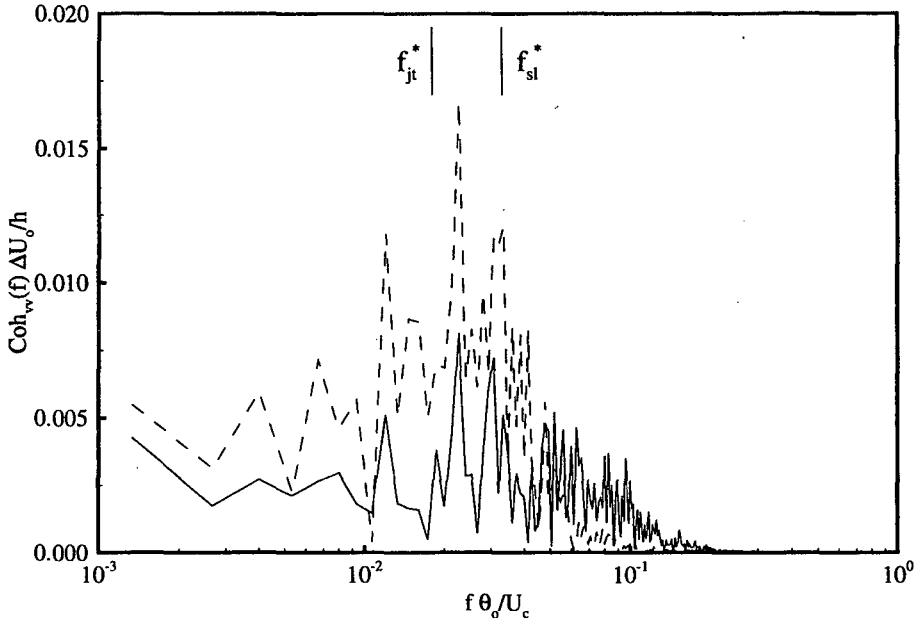

Figure 20: Two-point lateral velocity coherence spectra for points in the upper and lower shear layers, $y/\delta_U = \pm 1.0$, at the stations $x/h = 0.0$ and $x/h = 1.0$. ——$x/h = 0.0$, - - -$x/h = 1.0$.

using the shear layer scaling based on the inflow parameters. It is clear from the coherency spectra shown in figure 20 that the strongest growing mode between $x/h = 0.0$ and $x/h = 1.0$ is at a Strouhal number of $S = f\theta_o/U_c = 0.022$ based on the inflow conditions. If this scaling is based on the shear layer conditions at $x/h = 1.0$ the Strouhal number is 0.037. It is clear that the strong peak is a result of the shear layer instability and the frequency at which this mode occurs is affected by the increase in the shear layer momentum thickness between $x/h = 0.0$ and $x/h = 1.0$.

The secondary peak at $S = 0.012$ in figure 20 appears to be related to the subharmonic of the shear layer mode, although it does not occur at precisely one-half the Strouhal number of the strongest mode. The side peak at $S = f\theta_o/U_c = 0.018$ is consistent with the jet mode. In terms of the jet scaling, this mode occurs at a Strouhal number, $S = f\delta_U/\Delta U = 0.108$ which matches well with the experimentally observed jet mode of $S = f\delta_U/\Delta U = 0.11$. Figure 21 shows the coherency spectra of the lateral velocity at points on opposite sides of the jet at the stations, $x/h = 1.0$, 3.0 and 5.0 with the frequency normalized using the local jet scaling. The coherency spectra are scaled using the inflow parameters to prevent masking the growth of individual peaks. It is clear from this figure that the side peak mentioned above at the station $x/h = 1.0$ coincides closely with the jet mode. While the shear layer mode grows strongly between $x/h = 0.0$ and $x/h = 1.0$, downstream it is clear that the jet mode, $S = f\delta_U/\Delta U = 0.11$, becomes dominant. At $x/h = 5.0$ a strong peak has formed at frequencies near $S = f\delta_U/\Delta U = 0.10$. Although not shown here, the phase data corresponding to the strongest peak in the lateral velocity coherency spectra shifts from being out-of-phase at $x/h = 1.0$ to in-phase for $x/h = 5.0$. This indicates a transition from symmetric to asymmetric structures over this region of the jet. Downstream of $x/h = 5.0$, the coherency spectra maintains a broad peak coinciding with the jet mode. The corresponding phase data downstream indicates asymmetric structures.

Figure 22 shows the one-dimensional autospectra in time of the longitudinal velocity on the centerline of the jet at two stations downstream in the self-similar region. These spectra are scaled

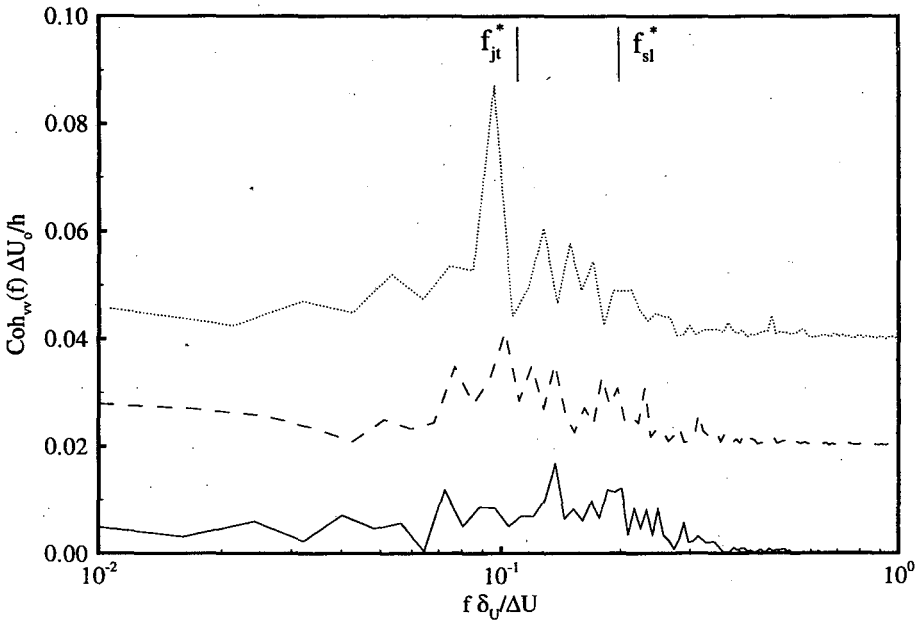

Figure 21: Two-point lateral velocity coherence spectra for points in the upper and lower shear layers, $y/\delta_U = \pm 1.0$, for $1.0 \leq x/h \leq 5.0$. —— $x/h = 1.0$, - - - $x/h = 3.0$, ····· $x/h = 5.0$.

using the local values for the jet-width, centerline velocity excess and the centerline variance of the longitudinal velocity. With this scaling, it is expected that the low wavenumber portion of the energy spectra in a fully developed jet would collapse. It can be seen in this figure that, for the conditions of this jet, all of the range of scales collapse relatively well. The energy spectra began exhibiting signs of self-similar behavior in the region near $x/h = 9.0$. The $k^{-5/3}$ law is plotted for comparison, although for the conditions of this simulation an extended inertial subrange is not observed in the energy spectra. However, there is clearly a dissipative region at high frequencies where the energy spectra decays at greater than a $k^{-5/3}$ rate.

Consistent with the earlier observation about the relative isotropy of the small scales in the fully developed region of the jet, the autospectra in time of the lateral and spanwise velocity components are very similar for the small-scale, high frequency, motions figure 23. However, as noted previously the large-scale, low frequency, motions are not similar between the two velocity components. A strong peak occurs in the autospectra of the lateral velocity component near the jet mode, $S = f\delta_U/\Delta U \approx 0.11$. Due to the symmetries associated with the isotropic turbulence assumption, the autospectra of the lateral and spanwise velocity components would be identical if the velocity fields were completely isotropic.

Between three and four orders-of-magnitude decay are present in both the temporal and the spanwise autospectra. This is large enough to indicate that the results are relatively well resolved.

5 Evolution of the Passive Scalar in a Three-Dimensional Turbulent Jet

There is a great interest in the transport and mixing processes of scalars in turbulent shear flows due to their importance in the propagation of contaminants in environmental flows, as well as the wide

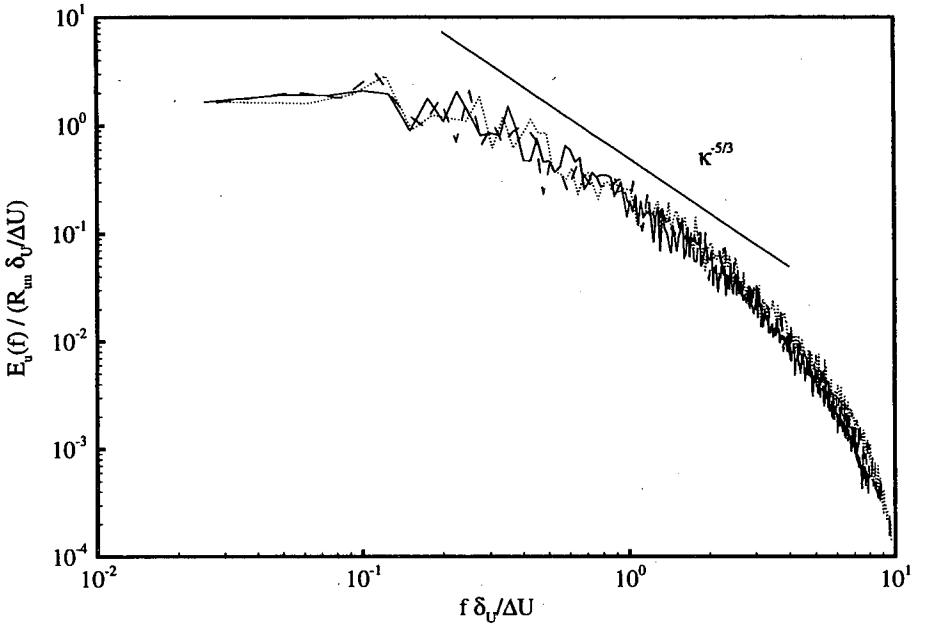

Figure 22: One-dimensional autospectra in time of the longitudinal velocity on the centerline in the self-similar region. —— $x/h = 10.0$, - - - $x/h = 11.0$, ····· $x/h = 12.0$.

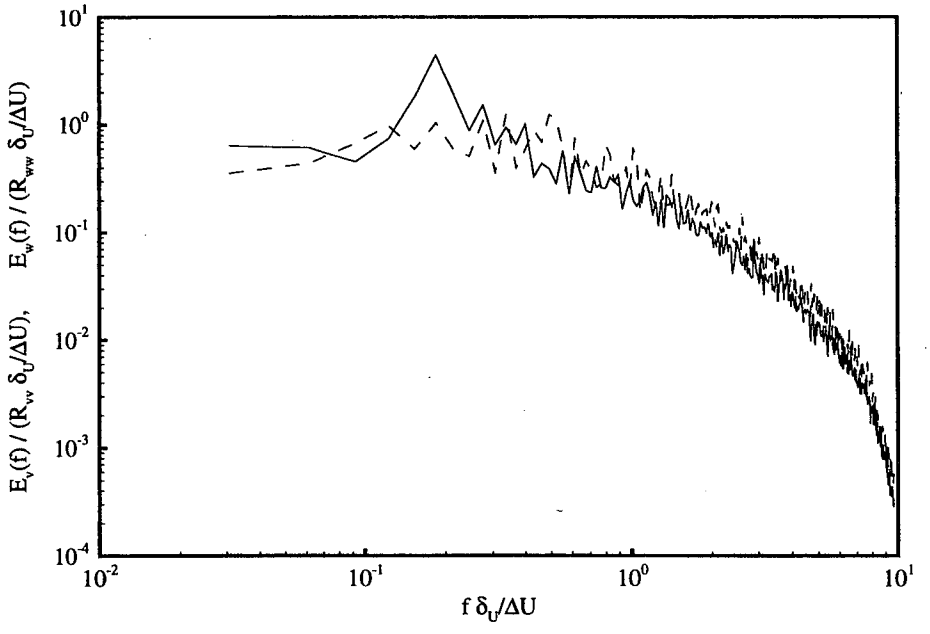

Figure 23: One-dimensional autospectra in time of the lateral and spanwise velocity components on the centerline in the self-similar region, $x/h = 12.0$. —— $E_v(f)$, - - - $E_w(f)$.

range of applications involving turbulent combustion. In an environmental application, a passive scalar can be used to represent a contaminant which is spread by the effects of the turbulent flowfield. Likewise, in the limit of fast chemistry, the effects of turbulent combustion can be modeled using a passive scalar.

The evolution of the passive scalar field in a $Re_h = 3000$ turbulent jet is discussed in this section. The physical conditions for this simulation match those of the previous jet except for a decrease in the inflow forcing intensity to 5% in the shear layers. This DNS was performed on the same computational grid as the previous simulation.

In the course of the discussion of the evolution of the passive scalar, comparison will be made against the experimental data of Ramaprian & Chandrasekhara (1985), Browne *et al.* (1983), Davies, Keffer & Baines (1975) as well as Jenkins & Goldschmidt (1973). In these studies the evolution of the "scalar" field was studied through experimental measurements of heated jets in air and water. In these studies the temperature difference between the jet and free stream fluids was kept small in order to minimize the effects of buoyancy on the evolution of the jet. Molecular effects on the evolution may be different since the Prandtl number, $Pr = C_p\mu/\kappa = 0.74$ for air and $Pr = 0.94$ for water while the Schmidt number used for the passive scalar in this jet is $Sc = 1.0$. However, the dominant means of scalar transport in turbulent jets is due to convection by the fluctuating velocity rather than due to molecular diffusion. Therefore, only the small-scale details, where molecular effects become significant, will be affected by this difference in Prandtl number without a major impact on the comparisons of scalar variables and fluxes made here. The physical conditions for the experimental studies utilized herein are given in table 1.

5.1 Visualization of the Passive Scalar Field

Figures 24 and 25 show instantaneous isocontours of the passive scalar on an xy-plane (side section) and a xz-plane (top section) in the jet, respectively, at a nondimensional time $t\Delta U_o/h = 89.10$. The xz-plane shown is at a station $y/h = 0.467$ which is just below the upper shear layer at the inflow. At this lateral station the fluid at the inflow is predominately jet fluid. In these figures, the contour levels are defined such that white indicates pure coflow fluid, $\widetilde{\xi} = 0.0$, while black indicates pure jet fluid, $\widetilde{\xi} = 1.0$. The levels of gray between are a measure of the mixedness of the fluid with darker indicating proportionally large quantities of jet fluid. The dark core of pure jet fluid is clearly evident in figure 24 near the inflow plane. In the region $x/h < 4.0$ there is a slight spreading of the core of the jet due to the effects of turbulent diffusion in the shear layers. At $x/h = 4.0$ a large-scale roll up is present in the upper and lower shear layers. The large-scale entrainment of coflow fluid by the upper structure is evident in figure 25 by the sudden appearance of a large region of white at $3.0 \leq x/h \leq 4.0$. While not entirely two-dimensional, as indicated by the inclination and spanwise inhomogeneity, the spanwise extent of this structure is large. In the region $5.0 \leq x/h \leq 7.0$ the remnants of a second structure can be seen in figure 24 and 25. As is evidenced by the medium gray shading of this structure in figure 25 the effects of small scale mixing have eliminated any region of pure coflow fluid entrained by this structure. Likewise, this structure has greater three-dimensionality than that of the structure nearer to the inflow.

Downstream in the jet, $x/h \geq 8.0$, the effects of small-scale mixing due to the strong turbulence in the jet have greatly reduced the presence of patches of pure jet and coflow fluid in the jet. However, there are small regions of fluid which are predominantly composed of one fluid type or the other. In figure 24 there is clearly a small patch composed primarily of jet fluid present near the jet centerline at $x/h = 11.0$. Likewise, near the jet edges there are clearly regions where nearly pure coflow fluid have been engulfed into the more mixed fluid present in the jet.

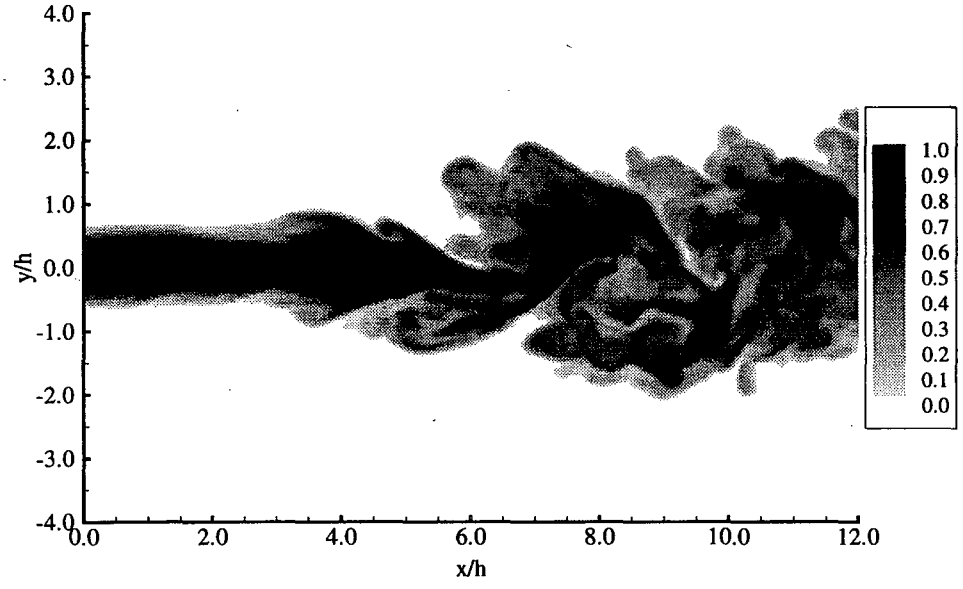

Figure 24: Instantaneous passive scalar contours on an xy-plane, $z = 0.0$.

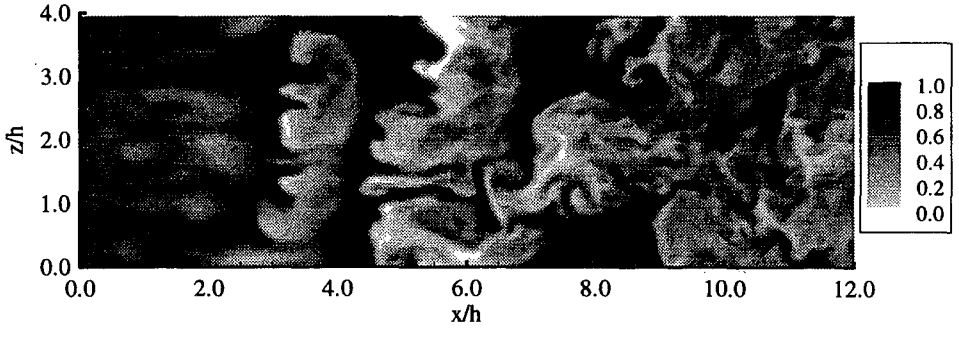

Figure 25: Instantaneous passive scalar contours on a xz-plane just below the upper shear layer, $y/h = 0.44$.

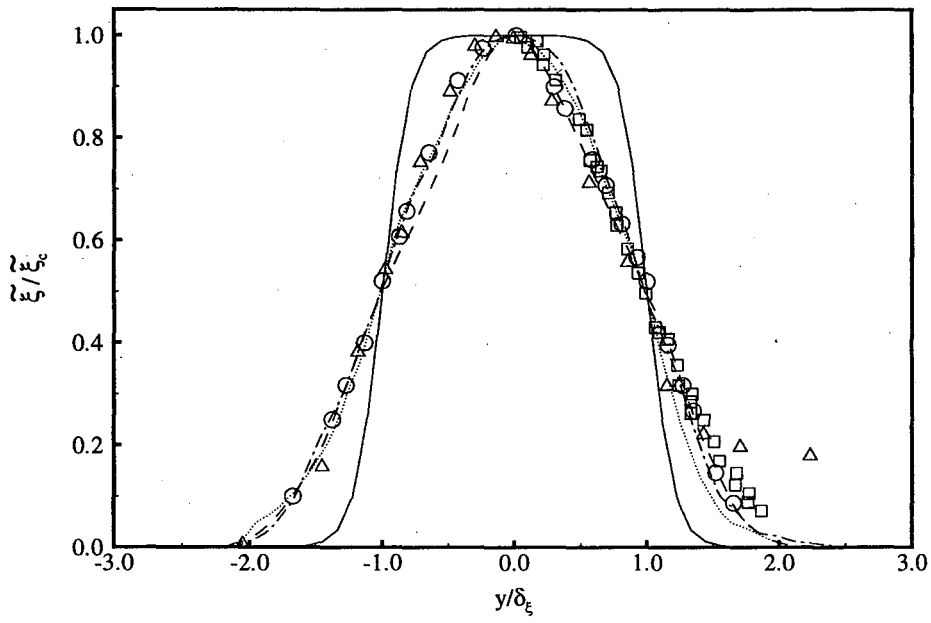

Figure 26: Mean scalar profiles in a planar jet. —— $x/h = 0.0$, - - - $x/h = 7.0$, — - — $x/h = 10.0$, ····· $x/h = 12.0$, □ Davies *et al.* (1975), △ Ramaprian & Chandrasekhara (1985), ○ Jenkins & Goldschmidt (1973).

5.2 Mean and Fluctuating Scalar Fields

Figure 26 shows the mean profiles of the passive scalar field at several streamwise stations. At the inflow plane, $x/h = 0.0$, the sharp transition from pure coflow fluid, $\widetilde{\xi} = 0.0$, to pure jet fluid, $\widetilde{\xi} = 1.0$, in the near field of the jet is evident. Downstream, the effects of strong turbulent mixing in the shear layers act to spread this profile until self-similarity is approached near $x/h = 7.0$. The mean passive scalar profiles are slightly slower to develop than the mean velocity field. The mean longitudinal velocity becomes self-similar at $x/h = 6.0$ in this jet. Due to the lower fluctuation intensity at the inflow, this jet develops slower than that discussed in § 4. The mean passive scalar profiles from DNS compare well with experimental profiles for the mean temperature excess of Ramaprian & Chandrasekhara (1985), Davies *et al.* (1975) as well as Jenkins & Goldschmidt (1973).

The self-similar scaling of the mean profiles in figure 26 masks the mixing and subsequent decay in the overall scalar values downstream in the jet. The decay in the mean value of the passive scalar on the jet centerline provides a measure of the overall mixing in the jet. Figure 27 shows the downstream variation in the centerline scalar values plotted using self-similar scaling. The symbols in this figure are experimental data for the centerline temperature decay in heated jets. The data of Browne *et al.* (1983) shows a very strong decay in the region $5.0 \leq x/h \leq 10.0$, followed by a slower linear decay downstream. In the DNS results for the passive scalar, a similar strong initial decay is observed.

The mathematical analysis for the self-similar region of the planar jet gives a downstream variation of the mean scalar on the centerline of $\widetilde{\xi}_c \propto x^{-1/2}$, similar to the centerline velocity decay. A linear fit of the values $(\widetilde{\xi}_o/\widetilde{\xi}_c)^2$ downstream in the jet, $x/h \geq 7.0$, results in the relationship

$$\left(\frac{\widetilde{\xi}_o}{\widetilde{\xi}_c}\right)^2 = C_{1\xi}\left[\frac{x}{h} + C_{2\xi}\right] \tag{31}$$

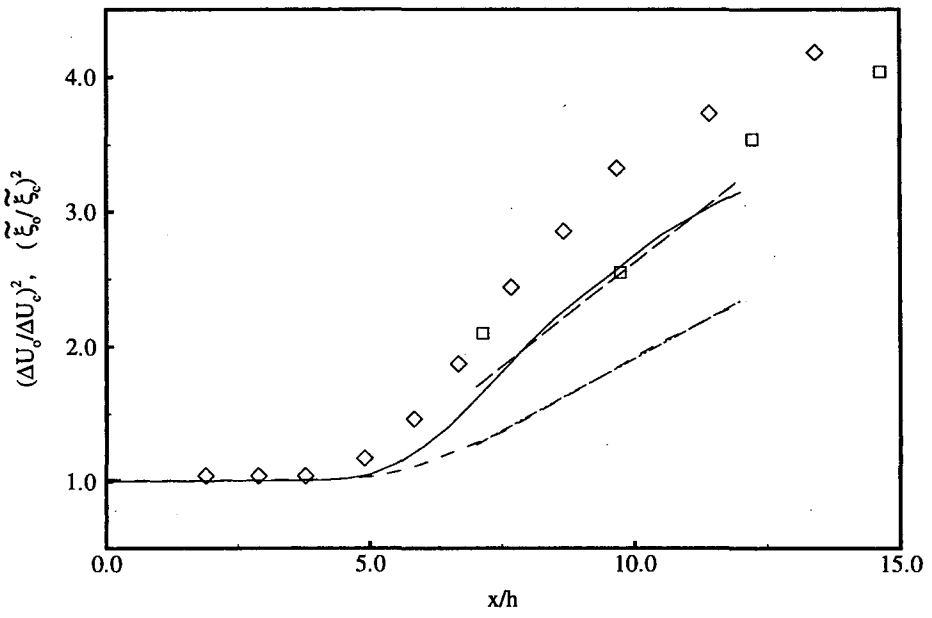

Figure 27: Decay of the mean scalar and centerline velocity excess on the jet centerline. —— $(\tilde{\xi}_o/\tilde{\xi}_c)^2$, - - - $(\Delta U_o/\Delta U_c)^2$, — — $(\tilde{\xi}_o/\tilde{\xi}_c)^2 = 0.308(x/h - 1.48)$, -·-· $(\Delta U_o/\Delta U_c)^2 = 0.213(x/h - 1.02)$, ◇ Browne *et al.* (1983), □ Davies *et al.* (1975).

where $C_{1\xi} = 0.308$ and $C_{2\xi} = -1.48$ for this jet. Table 7 shows a comparison of these constants to experimentally obtained values for the temperature field in heated jets. In general, the centerline scalar decay rates in the self-similar region, $x/h \geq 7.0$, are high compared to the experimental values. As noted above, Browne *et al.* (1983) show a large decay in the region $5.0 \leq x/h \leq 10.0$, however they do not observe self-similar decay, $\tilde{\xi} \propto x^{-1/2}$, until $x/h \geq 10.0$. The self-similar decay region from Browne *et al.* is only shown by the last three points in figure 27. It is reasonable that the decrease in the slope of the DNS scalar decay is a gradual shift into a slower more linear decay downstream.

Figure 28 shows the downstream growth in the jet half-width based on the mean profiles of the passive scalar. The symbols in this figure show experimentally measured values for the jet width based on the mean temperature profiles in a heated jet. The slow initial development of this jet to the linear growth rate, $\delta_\xi \propto x$, in the self-similar region is apparent. While Browne *et al.* (1983) see linear growth near $x/h = 3.0$, for the current case $x/h = 6.0$ before linear growth is observed, although the

Source	$K_{1\xi}$	$K_{2\xi}$	$C_{1\xi}$	$C_{2\xi}$	$K_{1u}/K_{1\xi}$	$C_{1u}/C_{1\xi}$
DNS, $q/\Delta U_o = 0.05$	0.158	-1.34	0.308	-1.48	0.66	0.69
Ramaprian & Chandrasekhara (1985)	0.167	2.00	0.194	6.00	0.66	0.87
Browne *et al.* (1983)	0.128	5.00	0.189	7.86	0.81	0.76
Jenkins & Goldschmidt (1973)	0.123	0.090	0.261	-5.62	0.71	0.61
Davies *et al.* (1975)	0.115	2.05	0.258	0.920	0.87	0.61

Table 7: Jet growth rates based on the passive scalar and centerline scalar decay rates for the current results and several experimental studies.

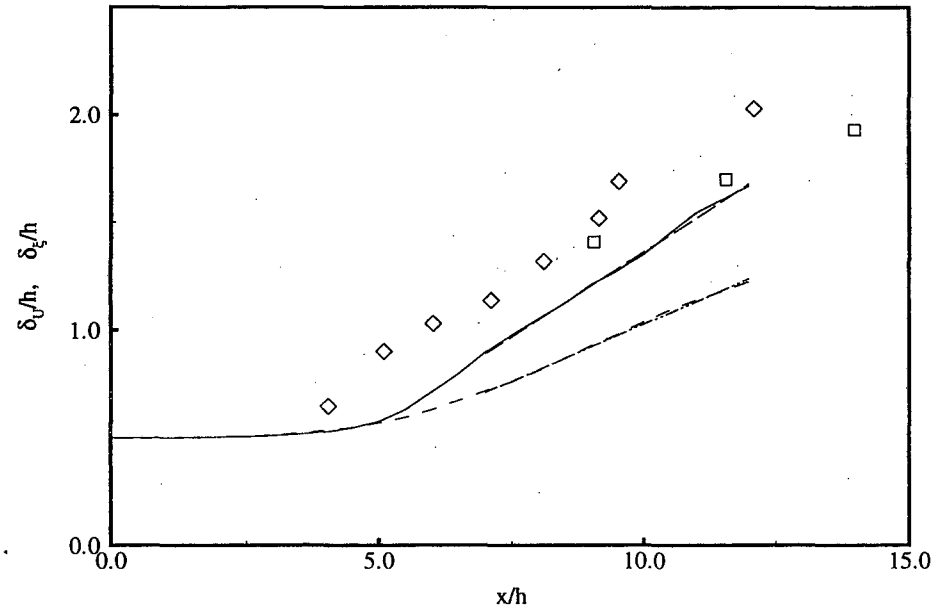

Figure 28: Downstream growth of the jet half-widths based on the passive scalar and velocity. —— δ_ξ/h, - - - δ_U/h, —— $\delta_\xi/h = 0.158(x/h - 1.34)$, -·-· $\delta_U/h = 0.105(x/h - 0.220)$, ◇ Browne *et al.* (1983), □ Davies *et al.* (1975).

self-similar growth rate downstream from the current results is consistent with experimental data. A fit of the scalar half-widths to the functional form

$$\frac{\delta_\xi}{h} = K_{1\xi}\left[\frac{x}{h} + K_{2\xi}\right] \tag{32}$$

gives the constants $K_{1\xi} = 0.158$ and $K_{2\xi} = -1.34$ for the current results. As can be seen in table 7, the linear growth rate, $K_{1\xi}$, compares well with the experimental data for heated jets. As with the virtual origins for the velocity field, there is a great deal of scatter in the values for the virtual origins of the scalar field, $K_{2\xi}$ and $C_{2\xi}$. These values are strongly affected by the nozzle conditions in the jet and thus vary considerably from one study to the next.

The decay of the centerline mean velocity excess and the jet half-width based on the velocity field for this case are also shown in figures 27 and 28. The constants in the fits for the self-similar development of δ_U/h and $(\Delta U_o/\Delta U_c)^2$ are $K_{1u} = 0.105$, $K_{2u} = -0.220$, $C_{1u} = 0.213$ and $C_{2u} = -1.02$, based on the region $x/h \geq 7.0$. The spread rates and centerline decay rates for the scalar field are larger than those for the velocity field. This would seem to indicate that the mixing of the scalar field occurs at a faster rate than for the velocity field. The ratio of scalar to velocity spread rates, $K_{1u}/K_{1\xi} = 0.66$, and scalar to velocity centerline decay rates, $C_{1u}/C_{1\xi} = 0.69$, are in the range of experimental values for the temperature field, table 7. In free shear flows, the turbulent Schmidt number, $Sc_t = \nu_t/D_t \approx 0.7$, which is consistent with the observed ratios $K_{1u}/K_{1\xi}$ and $C_{1u}/C_{1\xi}$ observed in the direct numerical simulation.

Figure 29 shows the downstream evolution of the centerline scalar fluctuation intensity, $R_{\xi\xi}$. Consistent with the slow initial development of this jet, the scalar fluctuation intensities evolve slower relative to experiment. The strong growth in the centerline intensities occurs at $x/h = 5.0$ for the current jet and is followed by a slow decay downstream, $x/h \geq 8.0$. Browne *et al.* (1983) observed a strong growth at $x/h = 4.0$ to a value greater than two times their downstream self-similar intensity. This peak was then followed by a slow decay downstream to the self-similar values

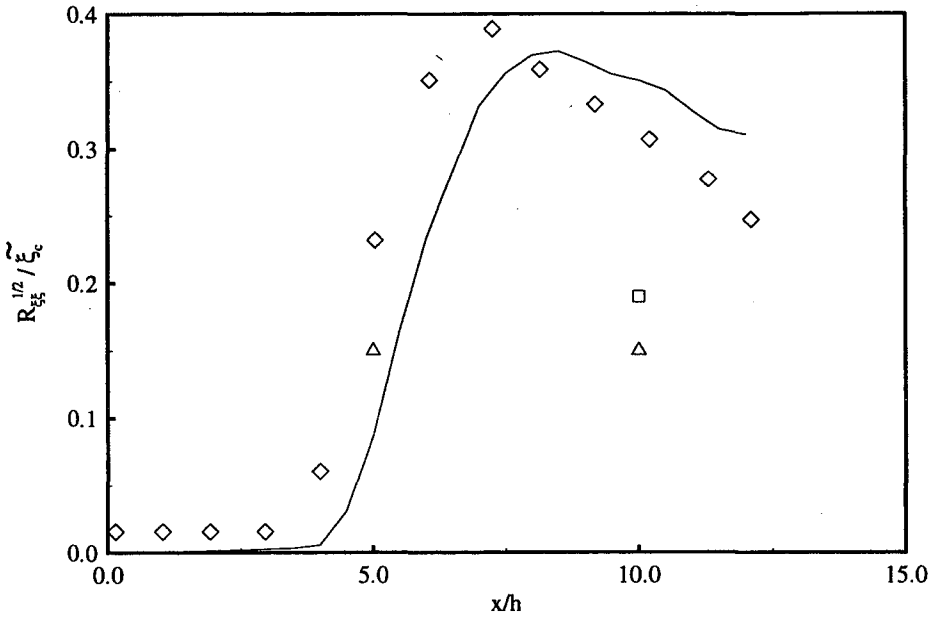

Figure 29: Growth of the scalar fluctuation intensity on the jet centerline. —— Current results, ◇ Browne *et al.* (1983), □ Davies *et al.* (1975), △ Ramaprian & Chandrasekhara (1985).

at $x/h = 15.0$, not shown in this figure. An overshoot in the velocity fluctuations is not observed in the current DNS or by Browne *et al.*.

5.3 Evolution of the Scalar Probability Density Functions

The evolution of the probability density functions, PDF, of a passive scalar has been utilized to study the mixing process in planar turbulent shear layers (Koochesfahani & Dimotakis, 1986; Batt, 1977; Rogers & Moser, 1994; Karasso & Mungal, 1996), as well as in round jets (for example Dahm & Dimotakis, 1990). However, there remains considerable debate on the final downstream state of the mixing process in self-similar shear layers.

The characterization of mixing through the use of probability density functions requires the definition of a classification scheme for the PDF. In the studies of mixing in turbulent shear layers, classification of the probability density functions into "marching", "non-marching" and "tilted" has been used (Rogers & Moser, 1994; Karasso & Mungal, 1996). In "marching" PDFs, the *most probable* value varies across the layer in a fashion closely following the *local mean* value for the scalar. This type of probability density function is characteristic of the classical notion of mixing dominated by the small scales of motion. "Non-marching" PDFs , on the other hand, are characterized by a most probable value which remains at a constant location across the layer irrespective of the local mean value. In non-marching PDFs, the primary peak is accompanied by a secondary peak corresponding to unmixed fluid from one stream or the other. This type of probability density function characterizes mixing which is dominated by large-scale engulfing of pure fluid from the external streams. The "tilted" type of probability density function which is a hybrid of the other two types was suggested by Karasso & Mungal (1996). In this type of PDF the most probable value varies across the mixing region, although not as strongly as in marching PDFs. In addition, secondary peaks corresponding to unmixed fluid are still present. This type of probability density function would seem to indicate large-scale engulfing of unmixed fluid from each stream coupled with strong mixing at the small

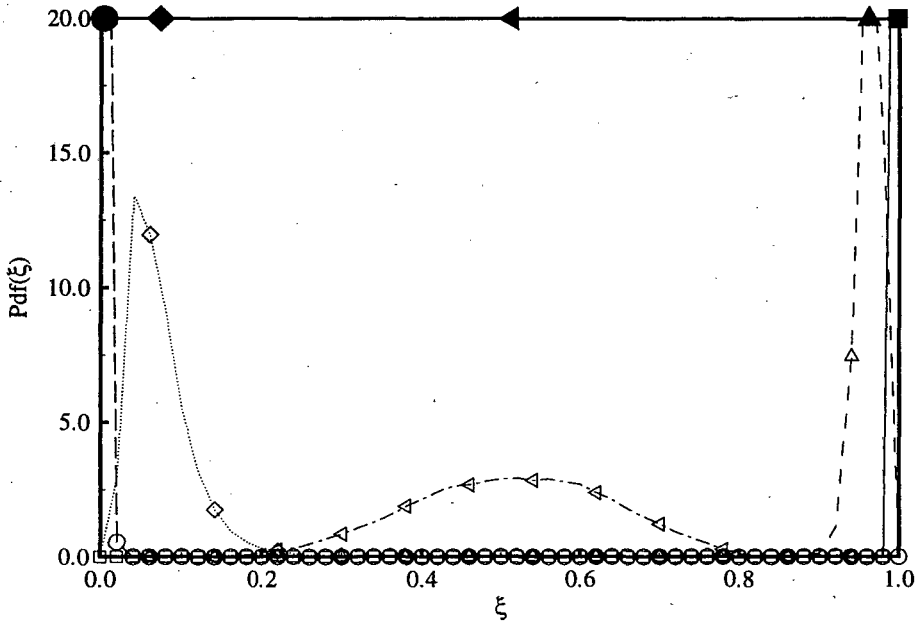

Figure 30: Variation of the probability density function of the passive scalar across the jet at $x/h = 1.0$. Symbols are as follows: $\square$ $y/\delta_\xi = 0.33$, $\triangle$ $y/\delta_\xi = 0.66$, $\triangleleft$ $y/\delta_\xi = 1.00$, $\diamond$ $y/\delta_\xi = 1.33$, $\bigcirc$ $y/\delta_\xi = 1.66$.

scales causing a shift in the most probable value.

While there has been considerable study of the scalar PDFs in turbulent shear layers and round jets, to the authors' knowledge there has been no such study in turbulent planar jets. As a building-block turbulent flow, understanding the mixing process in planar jets could be beneficial in a wide range of physical applications.

The variation of the probability density function of the passive scalar, Pdf(ξ), from the centerline of the jet outwards through the upper shear region is presented here in order to characterize the development of the mixing process in this jet. Figure 30 shows the PDF of the scalar for five lateral locations, $0.33 \leq y/\delta_\xi \leq 1.66$, at the streamwise station $x/h = 1.0$. In all of the PDFs presented, the solid symbols across the top of the plots give the mean scalar value for the PDF with the corresponding symbol. The station, $x/h = 1.0$, is very near the jet nozzle and thus the mixing process is dominated by the quasi-isotropic velocity fluctuations imposed at the inflow. The variation of the probability density functions across the jet at this station exhibit pure "marching" behavior where the peak in each PDF corresponds to the mean scalar value at that lateral location. The width of each PDF is a measure of the mixing due to the velocity fluctuations at that lateral location. As would be expected, the PDF at $y/\delta_\xi = 1.00$ is much wider than the others since the intensity of the velocity fluctuations peaks at $y/\delta_\xi \approx y/\delta_U = 1.0$. The PDF for $y/\delta_\xi = 0.33$ is characteristic of the behavior in $y/\delta_\xi < \pm 0.33$ at this streamwise station since pure jet fluid, $\xi = 1.0$, is present near the jet centerline.

Near the end of the potential core at $x/h = 4.0$ the probability density functions are very broad, figure 31. For the lateral location, $y/\delta_\xi = 1.05$, the mean scalar value is $\widetilde{\xi} = 0.47$. However, there is nearly equal probability of having any scalar value in the range $0.05 \leq \xi \leq 0.9$ with a drop in the probability for $\xi = 0.0$ and $\xi = 1.0$. For the lateral locations, $y/\delta_\xi = 0.52$ and 1.58, there is a high probability of having pure jet and pure coflow fluid, respectively, although the PDFs have a central broad region. This streamwise location is in the region where strong vortical structures

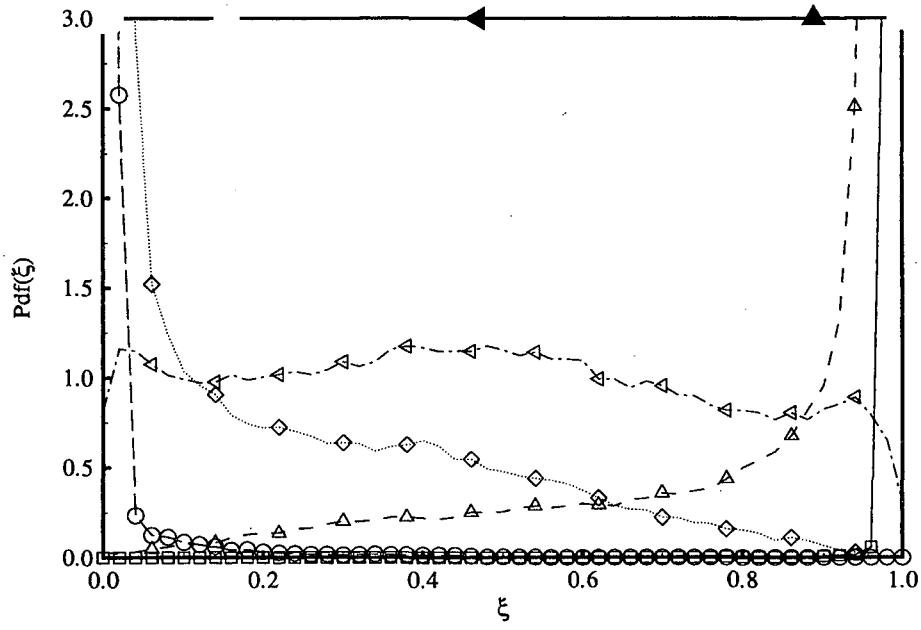

Figure 31: Variation of the probability density function of the passive scalar across the jet at $x/h = 4.0$. Symbols are as follows: $\square$ $y/\delta_\xi = 0.00$, $\triangle$ $y/\delta_\xi = 0.52$, $\triangleleft$ $y/\delta_\xi = 1.05$, $\diamond$ $y/\delta_\xi = 1.58$, $\bigcirc$ $y/\delta_\xi = 2.10$.

are beginning to develop, figure 24. It is likely that the broad range of scalar values present at $y/\delta_\xi = 1.05$ is due to the lateral motion of the region of sharp scalar gradient as vortical structures develop in the velocity field coupled with the occasional strong entrainment of coflow fluid by a structure that develops at $x/h < 4.0$.

Figure 32 shows the scalar PDFs across the jet at the station $x/h = 7.0$. This station is just downstream of the end of the potential core based on the velocity field and is the station at which the mean scalar profiles are beginning to show signs of self-similarity. At this station, the probability density functions for $y/\delta_\xi = 0.43$, 0.87 and 1.30 are decidedly *non-marching*. While the mean scalar values, solid shaded symbols at the top of the plot, vary strongly for $0.43 \leq y/\delta_\xi \leq 1.30$, a stationary central peak is present in the PDFs at scalar values $\xi \approx 0.5$. At each of these lateral stations there is a second strong peak in the probability density function corresponding to either pure jet fluid, $y/\delta_\xi = 0.43$, or pure coflow fluid, $y/\delta_\xi = 1.30$, or both $y/\delta_\xi = 0.87$. For all three PDFs, the secondary peaks are as strong or stronger than the central peak at $\xi \approx 0.5$. The probability density functions for $y/\delta_\xi = 0.0$ and 1.74 are quite broad and show a dominant peak of pure jet and pure coflow fluid, respectively. For $y/\delta_\xi = 0.0$ the mean scalar value is $\widetilde{\xi} = 0.79$, however the broad portion of the PDF only starts to decay for $\xi \leq 0.4$. The non-marching PDFs at this streamwise station, $x/h = 7.0$, indicates that, in this region of the jet, mixing is dominated by the large-scale engulfing of fluid. In the region $0.43 \leq y/\delta_\xi \leq 1.30$ away from the centerline and the jet edges, there is still a strong tendency to have patches of pure jet and pure coflow fluid, interspersed with mixed fluid.

Figure 33 shows the probability density functions of the passive scalar at the streamwise station $x/h = 9.0$ just before the fluctuating scalar and velocity fields reach self-similar behavior. The mean scalar value at the jet centerline at this station is $\widetilde{\xi} \approx 0.65$. However, even at this downstream station there is a high probability of finding pure jet fluid on the centerline. The strong peak corresponding to pure jet fluid in the PDF for $y/\delta_\xi = 0.41$ is significantly less than that which is present at

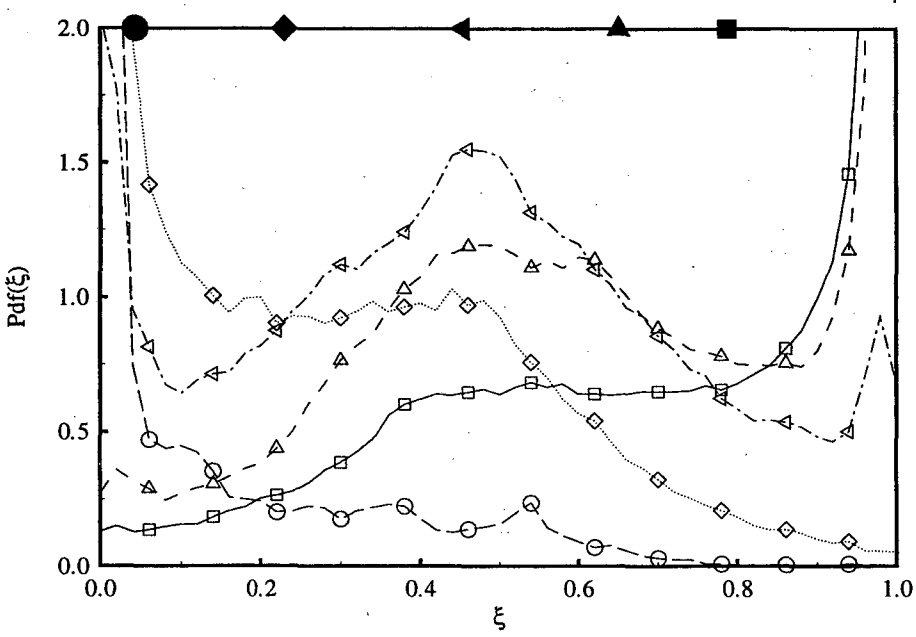

Figure 32: Variation of the probability density function of the passive scalar across the jet at $x/h = 7.0$. Symbols are as follows: $\Box$ $y/\delta_\xi = 0.00$, $\triangle$ $y/\delta_\xi = 0.43$, $\triangleleft$ $y/\delta_\xi = 0.87$, $\diamond$ $y/\delta_\xi = 1.30$, $\bigcirc$ $y/\delta_\xi = 1.74$.

$x/h = 7.0$ indicating a breakdown of the patches of pure jet fluid away from the centerline due to the effects of small-scale mixing. Thus, the fluid away from the jet axis is more thoroughly mixed with the coflow fluid than that on the axis.

The probability density function for $y/\delta_\xi = 0.78$ still shows the effects of large-scale engulfing of coflow and jet fluid. A strong central peak is present near $\xi = 0.42$ with secondary peaks corresponding to pure coflow,$\xi = 0.0$, and pure jet, $\xi = 1.0$, fluid. For $y/\delta_\xi = 1.15$ there is an even stronger indication of the large-scale entrainment of co-flow fluid. At this location there is relatively equal probability of finding fluid with $0.1 \leq \xi \leq 0.5$ as well as a very high probability for pure co-flow fluid. Comparison of the PDFs for $y/\delta_\xi = 0.0$, 0.41, 0.78 and 1.15 shows that there is some tendency of the central peak to shift from scalar values $\xi \approx 0.65$ to $\xi \approx 0.25$. This leads to the classification of these probability density functions as the "tilted" type, or a hybrid between marching and non-marching PDFs.

Figure 34 shows the probability density functions for the passive scalar field further downstream in the jet, $x/h = 11.5$, after the fluctuating velocity and scalar fields have obtained self-similar profiles. At this station, the PDF at the jet centerline no longer shows a strong peak corresponding to pure jet fluid, $\xi = 1.0$. Small-scale mixing has eliminated the presence of strong patches of unmixed jet fluid. The probability density functions at $y/\delta_\xi = 0.0$ and 0.38 exhibit "marching" type behavior at this streamwise station. There is a single peak in the PDF which corresponds to the mean value of the passive scalar at that lateral location.

At the lateral locations $y/\delta_\xi = 0.72$ and 1.07 the probability density functions of the passive scalar still show a central peak which tends to follow the local mean scalar value. However, at the stations in the outer half of the jet, closer to the coflow fluid, there are strong peaks in the PDFs corresponding to pure coflow fluid. At the outer point, $y/\delta_\xi = 1.45$, there is a sharp peak in the PDF corresponding to pure coflow fluid.

The picture of mixing in planar turbulent jets which is presented by these scalar probability

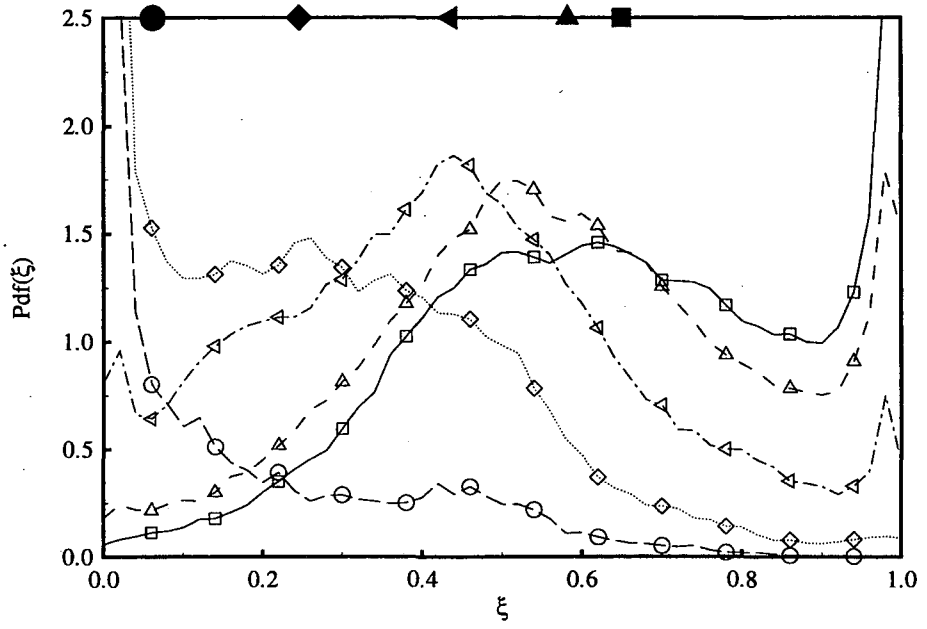

Figure 33: Variation of the probability density function of the passive scalar across the jet at $x/h = 9.0$. Symbols are as follows: □ $y/\delta_\xi = 0.00$, △ $y/\delta_\xi = 0.41$, ◁ $y/\delta_\xi = 0.78$, ◇ $y/\delta_\xi = 1.15$, ○ $y/\delta_\xi = 1.56$.

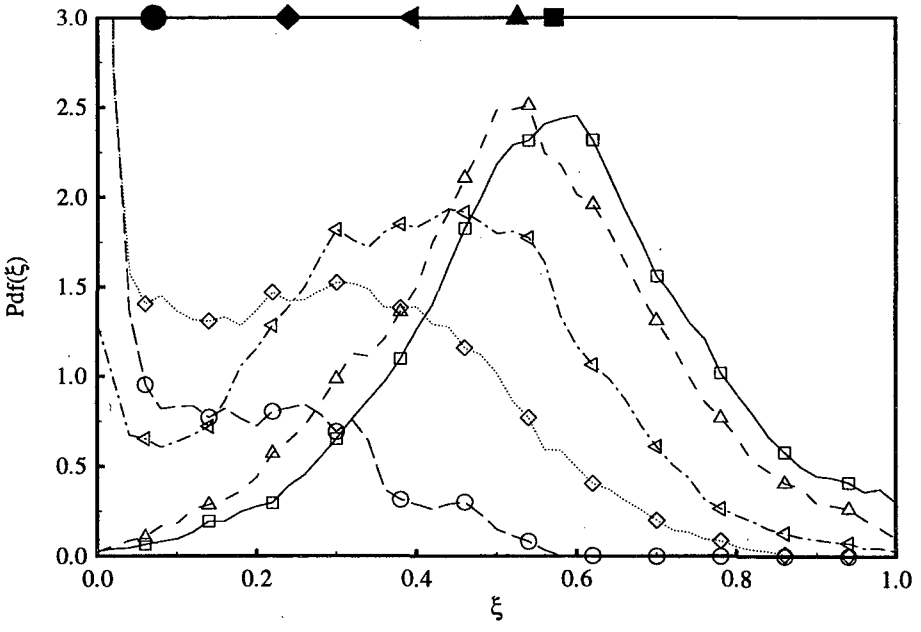

Figure 34: Variation of the probability density function of the passive scalar across the jet at $x/h = 11.5$. Symbols are as follows: □ $y/\delta_\xi = 0.00$, △ $y/\delta_\xi = 0.38$, ◁ $y/\delta_\xi = 0.72$, ◇ $y/\delta_\xi = 1.07$, ○ $y/\delta_\xi = 1.45$.

density functions is as follows. Near the jet nozzle, prior to the roll up of strong vortical structures, mixing is dominated by the effects of the quasi-isotropic turbulence imposed at the inflow. The probability density functions correspond to the classical marching type with the most probable value equal to the mean scalar value imposed at the inflow, with a widening of the PDFs in the shear layers due to the imposed small-scale motions. In the region of the jet, $4.0 \leq x/h \leq 5.0$, where strong vortical structures begin to develop in the shear layers, the mixing is still largely due to small-scale mixing, however there is a significant impact of the occasional large-scale transport of pure jet and coflow fluid across the interface by the randomly occurring large-scale structures. In a jet more strongly forced at the fundamental frequency for the shear layer, it is expected that the transition from the dominance of small-scale mixing, due to the imposed broadband inflow disturbances, to that of large-scale engulfing of fluid would be more dramatic and would occur at a fixed point in space. This type of forcing would lock the flowfield so that the roll up of large scale vortical structures occurs at a stationary point in space.

After strong vortical structures have developed, the mixing is dominated by the large-scale scale engulfing of pure jet and pure coflow fluid by these structures. The PDFs are of the "non-marching" or "tilted' type. However, as the flowfield in the core of the jet becomes more fully three-dimensional downstream, the influence of large-scale engulfing of fluid near the jet centerline, $y/\delta_\xi < 1.0$, becomes less significant. The mixing in the central core of the self-similar region of the jet is dominated by the effects of small-scale turbulent motion and exhibits "marching" probability-density-functions. However, near the edges of the jet, $y/\delta_\xi \geq 1.0$, the entrainment of pure coflow fluid due to the large-scale structures is still quite significant. The effects of small-scale mixing in the interior of the jet then break these patches up and transport the coflow fluid inward resulting in the downstream decay in the centerline values of the mean scalar.

6 Conclusions

A computational model has been developed for three-dimensional, spatially evolving, turbulent jets using direct numerical simulation of the compressible Navier-Stokes equations. This computational model utilizes state-of-the-art numerical techniques to deal with the complex issues in unsteady flow computations arising due to the open computational domain. The efficiency and accuracy, both temporal and spatial, of this computational model is suitable for performing detailed studies of spatially evolving turbulent flows. This numerical model provides detailed data on all flowfield variables in the initial and self-similar region of spatially evolving turbulent shear flows which, if validated against laboratory experiments, can be utilized in the evaluation and design of subgrid models for large-eddy simulation.

Three-dimensional simulations of the spatially evolving plane jet have been performed and results compared against the available experimental data. The self-similar jet growth rate, $K_{1u} = 0.093$, compares well with the values $K_{1u} = 0.110$ and $K_{1u} = 0.100$ observed experimentally by Ramaprian & Chandrasekhara (1985), and Gutmark & Wygnanski (1976), respectively. Likewise, the self-similar centerline velocity decay rate, $C_{1u} = 0.193$, agrees with the values $C_{1u} = 0.220$ measured by Thomas & Prakash (1991) and $C_{1u} = 0.189$ measured by Gutmark & Wygnanski (1976).

The mean longitudinal velocity profiles are self-similar at $x/h = 4.0$ and Reynolds stress profiles are approximately self-similar by $x/h = 10.0$. The self-similar mean and Reynolds stress profiles show good agreement with the experimental data of Ramaprian & Chandrasekhara (1985) as well as Gutmark & Wygnanski (1976). The growth of the fluctuating velocity components is in good agreement with experimental data, although there are some differences in the initial growth rate of the centerline root-mean-square longitudinal velocity. This, however, is not surprising since the downstream development of planar jets is sensitive to nozzle and external conditions. While the shear layer momentum thickness of the current results is somewhat larger than experimental values, the inflow fluctuation intensity has been designed to provide a rapid breakdown of the jet to a

fully-developed turbulent state. Unfortunately, insufficient data is available to match the inflow conditions in the direct numerical simulation exactly to the nozzle conditions in the experimental studies.

As shown through the use of coherency spectra across the jet, the simulation captures well the strong growth in the shear layer mode near the jet nozzle. A shifting of the dominant frequency in the coherency spectra is observed through the length of the potential core from the shear layer mode to that corresponding to the jet column mode. The transition to the dominance of the jet column mode occurs at the end of the potential core and thus coincides with the emergence of typical jet-like mean longitudinal velocity profiles. The region in which the jet column mode becomes dominant, $3.0 \leq /h \leq 5.0$, corresponds to that over which the strong breakdown to three-dimensionality occurs in the jet. Over this range, there is a substantial decrease of the longitudinal and spanwise correlation scales as well as a large increase in the energy content of the intermediate-to-small length scales in the turbulence.

The turbulent-kinetic-energy balance in the self-similar region from the DNS simulation generally compares well with those of Ramaprian & Chandrasekhara (1985) as well as Gutmark & Wygnanski (1976). Strong production is observed in the region of sharp mean gradient with turbulent transport towards the jet centerline and edges. The viscous dissipation is relatively uniform across the core of the jet, $-1 \leq y/\delta_U \leq 1$. The present results, however, have the advantage of allowing direct calculation of all terms in the TKE balance. While it is shown that on the centerline of the jet the small scales of motion are substantially more isotropic than at the jet edges, the isotropic approximation for the dissipation still underestimates the centerline value by 18%.

Comparisons have been made of the evolution of a passive scalar field in a planar turbulent jet to experimental data on the temperature field in heated planar jets. Self-similar mean scalar profiles compare well with mean temperature profiles from experimental studies. The initial evolution of the centerline scalar decay rate and jet width based on the passive scalar are somewhat slower in the current results due to differences between the inflow conditions in the DNS and experiments. However, the downstream growth rates and centerline decay rates compare well with experimental values.

Analysis of the probability density functions for the passive scalar has been used to characterize the evolution of the mixing process in turbulent planar jets. Near the nozzle, prior to vortex rollup, the probability density functions are dominated by the effects of quasi-isotropic small-scale fluctuations spreading the peaks of the PDFs. Therefore, in this region, scalar PDFs exhibit classical marching behavior. Downstream, after the roll up of strong vortical structures in the shear layers on either side of the potential core, the mixing process is dominated by large-scale engulfing of coflow fluid into the jet by these structures. In this region after vortex roll up, the probability density functions across the jet are non-marching.

However, when the flowfield in the jet becomes more fully turbulent downstream the influence of large-scale engulfing of fluid on the mixing near the jet centerline progressively decreases. In the core of the self-similar region of the jet, the mixing process is dominated by small-scale mixing. Therefore, the probability density functions of the passive scalar are of the marching type. However, near the jet edges, the engulfing of coflow fluid by the presence of large structures remains significant. Therefore, double peaks are present in the PDFs, one of which corresponds to pure fluid originating in the coflow.

In summary, the present work demonstrates through detailed comparison with classical experimental data that DNS with high-order space and time accuracy and appropriate schemes to handle inflow and outflow boundaries can successfully represent a spatially evolving plane jet. The development from interacting shear layers near the nozzle to the self-similar jet can be captured, albeit at a moderate Reynolds number. Such validated DNS can be useful in developing and validating improved turbulence prediction methods as well as in refining our knowledge of mixing in turbulent jets.

7 Acknowledgments

Support for the first author was provided by the Applied Mathematical Sciences Program of the DOE Office of Mathematics, Information, and Computational Sciences under contract DE-AC03-76SF00098 as well as by the Department of Energy Computational Sciences Graduate Fellowship Program. Partial support for the second author was provided by AFOSR through grant F49620-96-1-0106. This work was supported in part by a grant of HPC time from the Naval Oceanographic Office Department of Defense Major Shared Resource Center. In addition, this research used resources of the National Energy Research Scientific Computing Center, which is supported by the Office of Energy Research of the U.S. Department of Energy.

References

ALBERTSON, M. L., DAI, Y. B., JENSON, R. A. & HOUSE, H. 1950 Diffusion of submerged jets. *Trans. Am. Soc. Civ. Eng.* **115**, 639–664.

ANTONIA, R. A., BROWNE, L. W. B., RAJAGOPALAN, S. & CHAMBERS, A. J. 1983 On the organized motion of a turbulent plane jet. *J. Fluid Mech.* **134**, 49–66.

BASHIR, J. & UBEROI, M. S. 1975 Experiments on turbulent structure and heat transfer in a two-dimensional jet. *Phys. Fluids* **18** (4), 405–410.

BATT, R. G. 1977 Turbulent mixing of passive and chemically reacting species in a low-speed shear layer. *J. Fluid Mech.* **82** (1), 53–95.

BELL, J. H. & MEHTA, R. D. 1990 Development of a two-stream mixing layer from tripped and untripped boundary layers. *AIAA J.* **28** (12), 2034–2042.

BRADBURY, L. J. S. 1965 The structure of a self-preserving turbulent plane jet. *J. Fluid Mech.* **23** (1), 31–64.

BRADBURY, L. J. S. & RILEY, J. 1967 The spread of a turbulent jet issuing into a parallel moving airstream. *J. Fluid Mech.* **27** (2), 381–394.

BROWNE, L. W. B., ANTONIA, R. A., RAJAGOPALAN, S. & CHAMBERS, A. J. 1983 Interaction region of a two-dimensional turbulent plane jet in still air. In *Structure of Complex Turbulent Shear Flow* (ed. R. Dumas & L. Fulachier), *IUTAM Symp. Marseille 1982* , pp. 411–419. Springer.

CARPENTER, M. H., GOTTLIEB, D. & ABARBANEL, S. 1993 The stability of numerical boundary treatments for compact high-order finite-difference schemes. *J. Comput. Phys.* **108**, 272–295.

CARPENTER, M. H. & KENNEDY, C. A. 1994 Fourth-order 2n-storage Runge-Kutta schemes. NASA Technical Memorandum 109112. National Aeronautics and Space Administration, Langley Research Center, Hampton, VA 23681.

CERVANTES DE GORTARI, J. & GOLDSCHMIDT, V. W. 1981 The apparent flapping motion of a turbulent plane jet - further experimental results. *J. Fluids Engrg.* **103** (1), 119–126.

COMTE, P., LESIEUR, M., LAROCHE, H. & NORMAND, X. 1989 Numerical simulations of turbulent plane shear layers. In *Turbulent Shear Flows 6* (ed. J.-C. André, J. Cousteix, F. Durst, B. E. Launder, F. W. Schmidt & J. H. Whitelaw), pp. 361–380. Berlin: Springer-Verlag.

DAHM, W. J. A. & DIMOTAKIS, P. E. 1990 Mixing at large Schmidt number in the self-similar far field of turbulent jets. *J. Fluid Mech.* **217**, 299–330.

DAI, Y., KOBAYASHI, T. & TANIGUCHI, N. 1994 Large eddy simulation of plane turbulent jet flow using a new outflow velocity boundary condition. *JSME Internat. J.* **37** (2), 242–253.

DAVIES, A. E., KEFFER, J. F. & BAINES, W. D. 1975 Spread of a heated plane turbulent jet. *Phys. of Fluids* **18** (7), 770–775.

EVERITT, K. W. & ROBINS, A. G. 1978 The development and structure of turbulent plane jets. *J. Fluid Mech.* **88** (3), 563–583.

GOLDSCHMIDT, V. W. & BRADSHAW, P. 1973 Flapping of a plane jet. *Phys. Fluids* **16** (3), 354–355.

GOLDSCHMIDT, V. W., MOALLEMI, M. K. & OLER, J. W. 1983 Structures and flow reversal in turbulent plane jets. *Phys. Fluids* **26** (2), 428–432.

GUTMARK, E. & WYGNANSKI, I. 1976 The planar turbulent jet. *J. Fluid Mech.* **73** (3), 465–495.

HESKESTAD, G. 1965 Hot-wire measurements in a plane turbulent jet. *J. Appl. Mech.* **32** (4), 721–734.

HOFFMANN, G. & BENOCCI, C. 1994 Numerical simulation of spatially-developing planar jets. In *Applications of Direct and Large Eddy Simulation to Transition and Turbulence, AGARD-CP-551* , pp. 26.1–26.6. Advisory Group for Aerospace Research and Development, 7 Rue Ancelle, 92200 Neuilly-Sur-Seine, France.

HU, F. Q. 1996 On absorbing boundary conditions for linearized Euler equations by a perfectly matched layer. *J. Comput. Physics* **129** (1), 201–219.

HUSSAIN, A. K. M. F. & CLARK, A. R. 1977 Upstream influence on the near field of a plane turbulent jet. *Phys. Fluids* **20** (9), 1416–1426.

JENKINS, P. E. & GOLDSCHMIDT, V. W. 1973 Mean temperature and velocity in a plane turbulent jet. *J. Fluids Engrg.* **95** (4), 581–584.

JONES, W. P. & WILLE, M. 1996 Large-eddy simulation of a plane jet in a cross-flow. *Int. J. Heat and Fluid Flow* **17** (3), 296–306.

KARASSO, P. S. & MUNGAL, M. G. 1996 Scalar mixing and reaction in plane liquid shear layers. *J. Fluid Mech.* **323**, 23–63.

KOOCHESFAHANI, M. M. & DIMOTAKIS, P. E. 1986 Mixing and chemical reactions in a turbulent liquid mixing layer. *J. Fluid Mech.* **170**, 83–112.

KOTSOVINOS, N. E. 1977 Pane turbulent bouyant jets. part 2. turbulence structure. *J. Fluid Mech.* **81** (1), 45–62.

KOTSOVINOS, N. E. & LIST, E. J. 1977 Plane turbulent bouyant jets. part 1. integral properties. *J. Fluid Mech.* **81** (1), 25–44.

LARUE, J. C., LY, T., RAHAI, H. & JAN, P. Y. 1997 On similarity of a plane turbulent jet in a co-flowing stream. In *Proceedings Eleventh Symposium on Turbulent Shear Flows*, , vol. 3, pp. 25.11–25.16. Grenoble, France: Springer-Verlag.

LASHERAS, J. C. & CHOI, H. 1988 Three-dimensional instability of a plane free shear layer: An experimental study of the formation and evolution of streamwise vortices. *J. Fluid Mech.* **189**, 53–86.

LE RIBAULT, C., SARKAR, S. & STANLEY, S. A. 1998 Large eddy simulation of a plane jet. *Submitted to Phys. Fluids* .

LELE, S. K. 1992 Compact finite difference schemes with spectral-like resolution. *J. Comput. Phys.* **103**, 16–42.

LEMIEUX, G. P. & OOSTHUIZEN, P. H. 1985 Experimental study of the behaviour of plane turbulent jets at low Reynolds numbers. *AIAA J.* **23** (12), 1845–1846.

MICHALKE, A. 1965 On spatially growing disturbances in an inviscid shear layer. *J. Fluid Mech.* **23** (3), 521–544.

MICHALKE, A. & FREYMUTH, P. 1966 The instability and the formation of vortices in a free boundary layer. In *Separated Flows, Part 2, AGARD Conference Proceedings 4* , pp. 575–595. Advisory Group for Aerospace Research and Development, 64 Rue De Varenne, Paris, France.

MILLER, D. R. & COMINGS, E. W. 1957 Static pressure distributions in the free turbulent jet. *J. Fluid Mech.* **3**, 1–16.

MONKEWITZ, P. A. & HUERRE, P. 1982 Influence of the velocity ratio on the spatial instability of mixing. *Phys. Fluids* **25** (7), 1137–1143.

MUMFORD, J. C. 1982 The structure of the large eddies in fully developed turbulent shear flows. Part 1: The plane jet. *J. Fluid Mech.* **118**, 241–268.

NAMER, I. & ÖTÜGEN, M. V. 1988 Velocity measurements in a plane turbulent air jet at moderate Reynolds numbers. *Exp. Fluids* **6**, 387–399.

OLER, J. W. & GOLDSCHMIDT, V. W. 1982 A vortex-street model of the flow in the similarity region of a two-dimensional free turbulent jet. *J. Fluid Mech.* **123**, 523–535.

OLER, J. W. & GOLDSCHMIDT, V. W. 1984 Coherent structures in the similarity region of two-dimensional turbulent jets. *ASME J. Fluids Engrg.* **106**, 187–192.

POINSOT, T. J. & LELE, S. K. 1992 Boundary conditions for direct simulations of compressible viscous flows. *J. Comput. Phys.* **101**, 104–129.

RAMAPRIAN, B. R. & CHANDRASEKHARA, M. S. 1985 LDA measurements in plane turbulent jets. *ASME J. Fluids Engrg.* **107**, 264–271.

REICHERT, R. S. & BIRINGEN, S. 1997 Numerical simulation of compressible plane jets. *AIAA Paper 97-1924* .

ROCKWELL, D. O. & NICCOLLS, W. O. 1972 Natural breakdown of planar jets. *Trans. ASME: J. Basic Engrg.* **1**, 720–730.

ROGERS, M. M. & MOSER, R. D. 1994 Direct simulation of a self-similar turbulent mixing layer. *Phys. Fluids* **6** (2), 903–923.

RUDY, D. H. & STRIKWERDA, J. C. 1980 A nonreflecting outflow boundary condition for subsonic Navier-Stokes calculations. *J. Comput. Phys.* **36**, 55–70.

SATO, H. 1960 The stability and transition of a two-dimensional jet. *J. Fluid Mech.* **7** (1), 53–80.

SPENCER, B. W. & JONES, B. G. 1971 Statistical investigation of pressure and velocity fields in the turbulent two-stream mixing layer. *AIAA Paper 71-613* .

STANLEY, S. & SARKAR, S. 1997*a* Simulations of spatially developing plane jets. *AIAA Paper 97-1922* .

STANLEY, S. & SARKAR, S. 1997*b* Simulations of spatially developing two-dimensional shear layers and jets. *Theoret. Comput. Fluid Dynamics* **9**, 121–147.

STANLEY, S. A. & SARKAR, S. 1999 Direct numerical simulation of the developing region of turbulent planar jets. *AIAA Paper 99-0288* .

TENNEKES, H. & LUMLEY, J. L. 1972 *A First Course in Turbulence*. The MIT Press.

THOMAS, F. O. & CHU, H. C. 1989 An experimental investigation of the transition of a planar jet: Subharmonic suppression and upstream feedback. *Phys. Fluids A* **1** (9), 1566–1587.

THOMAS, F. O. & GOLDSCHMIDT, V. W. 1986*a* Acoustically induced enhancement of widening and fluctuation intensity in a two-dimensional turbulent jet. *ASME J. Fluids Engrg.* **108**, 331–337.

THOMAS, F. O. & GOLDSCHMIDT, V. W. 1986*b* Structural characteristics of a developing turbulent planar jet. *J. Fluid Mech.* **163**, 227–256.

THOMAS, F. O. & PRAKASH, K. M. K. 1991 An experimental investigation of the natural transition of an untuned planar jet. *Phys. Fluids A* **3** (1), 90–105.

THOMPSON, K. W. 1987 Time dependent boundary conditions for hyperbolic systems. *J. Comput. Phys.* **68**, 1–24.

THOMPSON, K. W. 1990 Time-dependent boundary conditions for hyperbolic systems ii. *J. Comput. Phys.* **89**, 439–461.

WEINBERGER, C., REWERTS, J. & JANICKA, J. 1997 The influence of inlet conditions on a large eddy simulation of a turbulent plane jet. In *Proceedings Eleventh Symposium on Turbulent Shear Flows*, , vol. 3, pp. 25.17–25.22. Grenoble, France: Springer-Verlag.

WILLIAMS, F. A. 1985 *Combustion Theory*, 2nd edn. New York: Addison-Wesley.

WYGNANSKI, I. & FIEDLER, H. E. 1970 The two-dimensional mixing region. *J. Fluid Mech.* **41** (2), 327–361.

ZALESAK, S. T. 1979 Fully multidumensional flux-corrected transport algorithms for fluids. *J. Comp. Phys.* **31** (3), 335–362.

Ernest Orlando Lawrence Berkeley National Laboratory
One Cyclotron Road · Berkeley, California 94720

Prepared for the U.S. Department of Energy under Contract No. DE-AC03-76SF00098